minerals

MDPI

Article

The Orogeny Transition of the Southern Beishan Orogenic Belt During the Early–Middle Devonian: Evidence from the Wudaomingshui Volcanic Rocks and Granite

Tongtong He [1,2,3], Yuxi Wang [1,2,4], Jing Yan [1,2], Zhiyong Yang [1,2], Kangning Li [1,2,3], Zirui Liu [3,5], Zixuan Wang [1,2] and Lei Wu [6,*]

[1] The Third Geological and Mineral Exploration Institute of Gansu Province Bureau of Geology and Mineral Resources, Lanzhou 730000, China; hett2024@lzu.edu.cn (T.H.); wangyx15@lzu.edu.cn (Y.W.); mn893@126.com (J.Y.); zhiyong011054@163.com (Z.Y.); likn2023@lzu.edu.cn (K.L.); 19993072136@163.com (Z.W.)
[2] Gold Mine Resource Exploration and Utilization Technology Innovation Center of Gansu Province, Lanzhou 730050, China
[3] College of Earth and Environmental Sciences, Lanzhou University, Lanzhou 730000, China; liuzr851985@163.com
[4] Geological Survey of Gansu Province, Lanzhou 730000, China
[5] Key Laboratory of Mineral Resources in Western China (Gansu Province), School of Earth Science, Lanzhou University, Lanzhou 730000, China
[6] Geological Hazards Prevention Institute, Gansu Academy of Sciences, Lanzhou 730000, China
* Correspondence: wul20@lzu.edu.cn

Abstract: The Southern Beishan Orogenic Belt (SBOB), an integral part of the Southern Central Asian Orogenic Belt (CAOB), is characterized by extensive Late Paleozoic magmatism. These igneous rocks are the key to studying the tectonic evolution process and the ocean–continent tectonic transformation in the southern margin of the CAOB and Paleo-Asian Ocean. We present zircon U-Pb chronology, in situ Lu-Hf isotopes, and whole-rock geochemistry data for Early–Middle Devonian volcanic rocks in the Sangejing Formation and granites from the Shuangyingshan-Huaniushan (SH) unit in the SBOB. The Wudaomingshiu volcanic rocks (Ca. 411.5 Ma) are calc-alkaline basalt-basaltic andesites with low SiO_2 (47.35~55.59 wt.%) and high TiO_2 (1.46~4.16 wt.%) contents, and are enriched in LREEs and LILEs (e.g., Rb, Ba, and Th), depleted in HREEs and HFSEs (Nb, Ta, and Ti), and weakly enriched in Zr-Hf. These mafic rocks are derived from the partial melting of the depleted lithosphere metasomatized by subduction fluid and contaminated by the lower crust. Wudaomingshui's high-K calc-alkaline I-type granite has a crystallization age of 383.6 ± 2.2 Ma (MSWD = 0.11, n = 13), high Na_2O (3.46~3.96 wt.%) and MgO (1.25~1.68 wt.%) contents, and a high DI differentiation index (70.69~80.45); it is enriched in LREEs and LILEs (e.g., Rb, Ba, and Th) and depleted in HREEs and HFSEs (e.g., Nb, Ta, and Ti). Granites have variable zircon $\varepsilon_{Hf}(t)$ values (−2.5~3.3) with Mesoproterozoic T_{DM2} ages (1310~1013 Ma) and originated from lower crustal melting with mantle inputs and minor upper crustal assimilation. An integrated analysis of magmatic suites in the SBOB, including rock assemblages, geochemical signatures, and zircon $\varepsilon_{Hf}(t)$ values (−2.5 to +3.3), revealed a tectonic transition from advancing to retreating subduction during the Early–Middle Devonian.

Keywords: Early–Middle Devonian; orogeny transition; monzogranite; Sangejing Formation; Beishan orogenic belt

check for updates

Academic Editor: Urs Klötzli

Received: 12 March 2025
Revised: 25 May 2025
Accepted: 4 June 2025
Published: 10 June 2025

Citation: He, T.; Wang, Y.; Yan, J.; Yang, Z.; Li, K.; Liu, Z.; Wang, Z.; Wu, L. The Orogeny Transition of the Southern Beishan Orogenic Belt During the Early–Middle Devonian: Evidence from the Wudaomingshui Volcanic Rocks and Granite. *Minerals* **2025**, *15*, 632. https://doi.org/10.3390/min15060632

Copyright: © 2025 by the authors. Licensee MDPI, Basel, Switzerland. This article is an open access article distributed under the terms and conditions of the Creative Commons Attribution (CC BY) license (https://creativecommons.org/licenses/by/4.0/).

1. Introduction

The Central Asian Orogenic Belt (CAOB), bounded by the Tarim, Siberian, North China, and East European cratons, constitutes the largest Phanerozoic accretionary orogenic belt in the world and was formed through Phanerozoic subduction–accretion processes [1–6]. This orogenic belt recorded the process of the Paleo-Asian Ocean form formation to subduction and extinction. A large number of oceanic crust fragments of the PAO and magmatic–metamorphic–sedimentary activities produced in the process of accretion orogeny in the CAOB [7–11], making the CAOB a pivotal region for elucidating geodynamic transitions during the evolution of the PAO [4,12,13].

Located in the southern margin of the middle segment of the CAOB is the Beishan Orogenic Belt (BOB), which links the Chinese Tianshan Orogenic Belt westward and the Solonker Suture Zone eastward (Figure 1a). The BOB serves as a natural laboratory for unraveling the tectonic evolution of the PAO and is composed of a series of magmatic arcs, microcontinents, ophiolites, accretionary wedges, and others [14]. The tectonic evolution of the BOB is related to the east–west tectonic connection and evolution within the CAOB and is influenced by the interaction between the tectonic domains of the PAO and Tethys. This special tectonic position makes the BOB crucial for studying the mode and time span of accretionary orogeny in the CAOB, as well as the tectonic pattern of NW China [15]. The BOB hosts four north–south-aligned ophiolite belts [Hongshishan (HOB), Jijitaizi-Xiaohuangshan (JXOB), Hongliuhe-Niujuanzi-Xichangjing (HNXOB), Huitongshan-Zhangfangshan (HZOB)] (Figure 1b). Taking the HNXOB as the boundary, the BOB is divided into the Northern BOB (NBOB) and the Southern BOB (SBOB). (Figure 1b). Magmatic rocks formed in different tectonic settings are the key to studying the tectonic evolution of the SBOB and the southern margin of the central PAO [5]. Geochronological data reveal two distinct magmatic events in the SBOB: the early Paleozoic and the Late Paleozoic [16–18].

The Early Paleozoic igneous rocks were formed during the subduction and convergence of the PAO and have geochemical characteristics of arc magmatic rocks [19,20]. However, there are many debates on the formation environment of the late magmatism because of the diversity of magmatic rock types and the complexity of geochemical characteristics of these rocks [21,22], and there is debate as to whether the SBOB was in an extensional setting or convergent setting during the Devonian [8,15]. Some scholars believe that the SBOB was in a post-collisional setting during the Devonian based on the evidence of A-type granites and within-plate basalts (WPBs) outcrop in the western section of the SBOB [5,7,18,23]. However, others also suggest that the SBOB is still dominated by subduction in the Devonian on the basis of arc-like igneous rocks [8,16,24,25]. These controversies hinder the correct understanding of the evolution process of the southern margin of the central PAO.

While Devonian magmatic rocks are widespread across the SBOB, earlier investigations have largely concentrated on its western portion. Conversely, the eastern sector of this region exhibits Devonian igneous outcrops that remain comparatively understudied in the existing literature [5]. A comprehensive analysis of eastern SBOB Devonian magmatism is essential for elucidating the transition from subduction-related to extensional tectonic settings and the oceanic-continental transformation along the central PAO's southern margin.

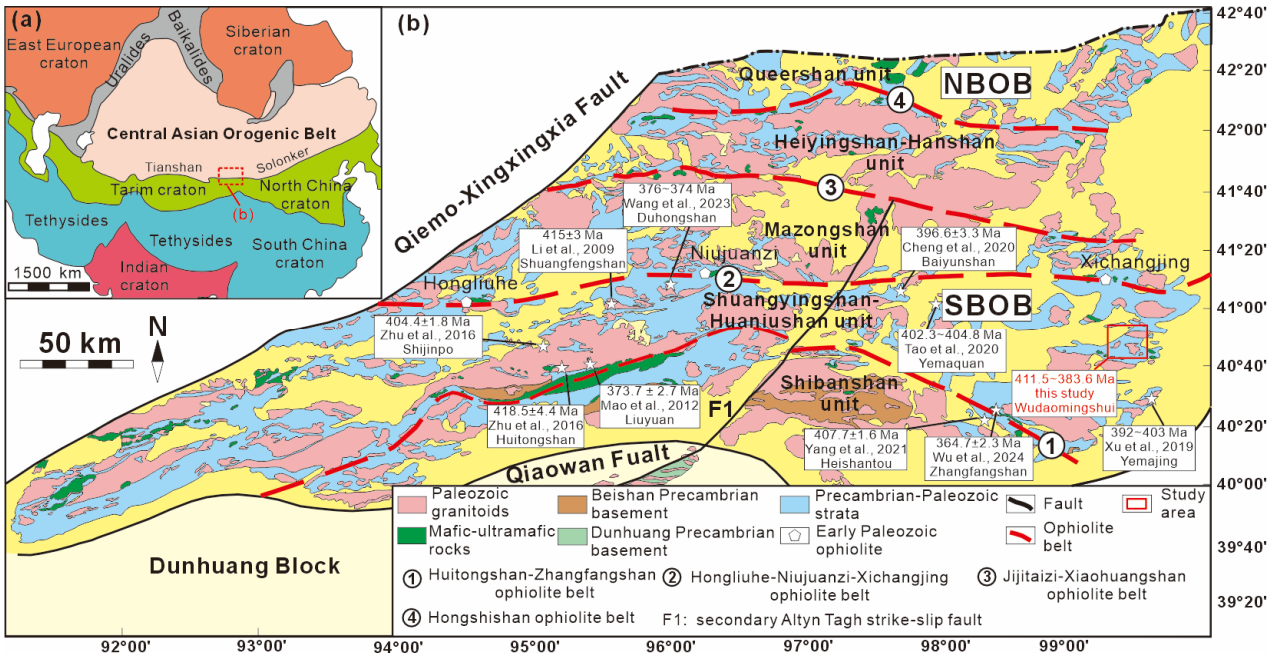


Figure 1. (**a**) A simplified tectonic map of the Central Asian Orogenic Belt (modified after [16]). (**b**) The geological framework of the BOB (modified after [12]). Age data of Devonian magmatic rocks from [5,8,18,19,21,23,24,26,27].

2. Geological Setting

The SBOB is comprises the Shibanshan unit, the Shuangyingshan-Huaniushan (SH) unit, and the HZOB is situated between these two units (Figure 1b).

The study area is located in the SH unit, in which the Proterozoic to Cenozoic strata are distributed. The northern part of the SH unit is predominantly composed of Proterozoic-Ordovician strata, which are composed of metamorphic rocks (including orthometamorphite and parametamorphite) and sedimentary rocks [7,16,25,28,29]. The Ordovician-Devonian strata are mainly outcrops in the southern part of the SH unit [5,17], and the lower Sangejing (SGJ) Formation and upper Dundunshan Formation are composed of the Devonian strata. The SGJ Formation is mainly composed of amygdaloidal basalt, andesite porphyrite, quartz keratophyre, and sandstone with siltstone and conglomerate [22,30]. In addition to the widespread of the Devonian strata, the felsic and mafic intrusive rocks formed in the Devonian are also widely outcrops in the SH unit [18,21,23,31]. These basic-acid intrusive rocks have a lower degree of metamorphic deformation than the Early Paleozoic magmatic rocks with obvious metamorphic deformation in the SH unit.

Volcanic rocks of the SGJ Formation and granites are exposed in the Wudaomingshui (WDMS) area in the east of the SH unit (Figure 1b). The Precambrian Dunhuang Group and Gudongjing Group, the lower Devonian SGJ Formation, the Upper Carboniferous-lower Permian Ganquan Formation, the middle Jurassic toutunhe Formation, the lower Cretaceous Chijinbao Formation and Quaternary outcropping in the WDMS (Figure 2a). The SGJ Formation is composed of amygdaloidal basalt, trachybasalt, andesite, siltstone, sandstone, mudstone, and siliceous rock. This formation forms an unconformable contact with the Dunhuang Group, Ganquan Formation, Chijinbao Formation, and Quaternary, and is invaded by Permian quartz diorite (Figures 2b and 3a,b). Because of strongly weathering, the rocks of the SGJ Formation are generally broken (Figure 3b). The Ordovician, Silurian, Devonian, and Permian quartz diorite, granodiorite, and granite are also outcrop in the study area. The Devonian granite intrudes into the Ordovician quartz diorite and Silurian granodiorite (Figures 2a and 3c,d).

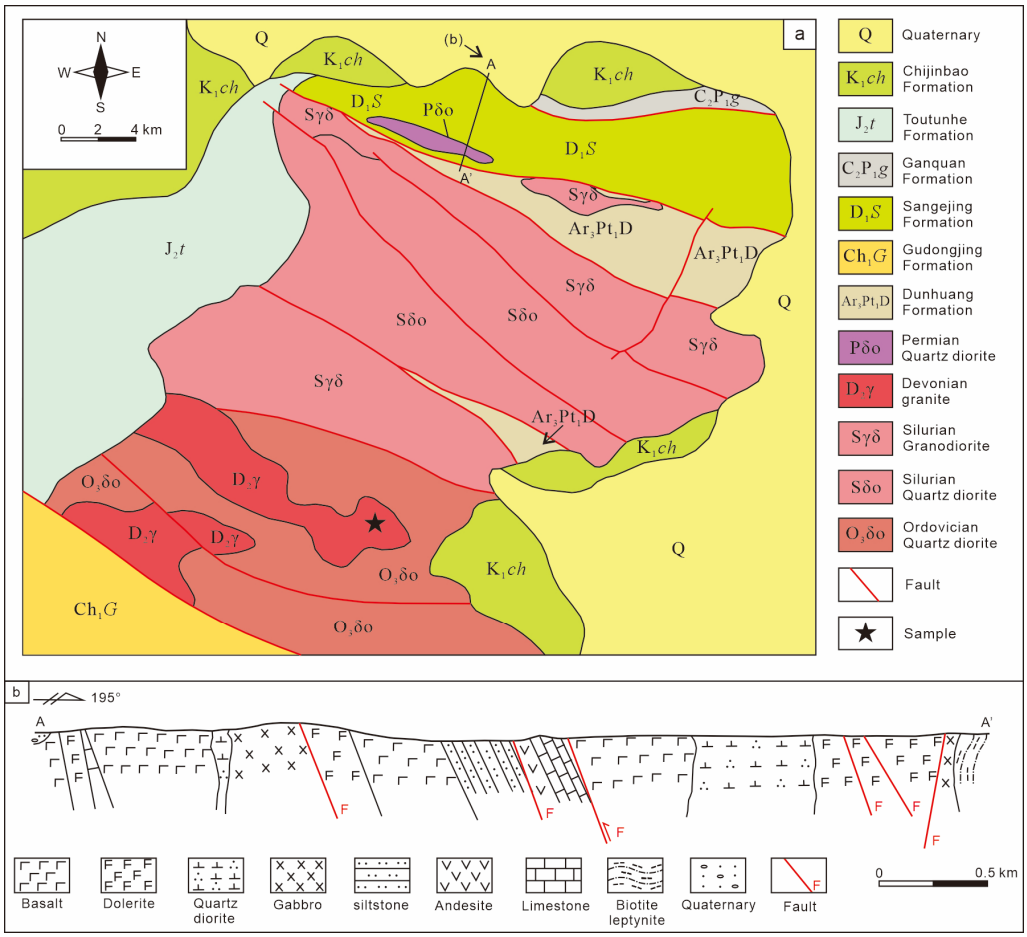


Figure 2. (**a**) Geological map of the Wudaomingshui (WDMS) area; (**b**) profile of the Sangejing Formation.

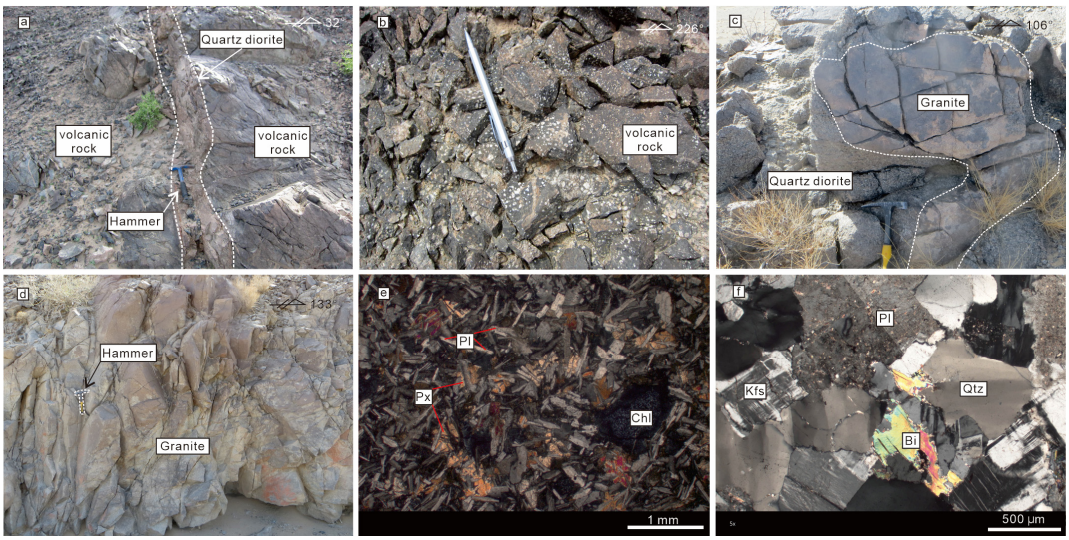


Figure 3. Field photos and microphotographs showing the geological and petrographical features of the WDMS volcanic rock and granite. (**a**) The Quartz diorite intruded into the volcanic rock; (**b**) volcanic rocks within the SGJ Formation display characteristic amygdaloidal textures; (**c**) granite intruded into the Quartz diorite; (**d**) Field photograph of the granite; (**e**) mineral compositions of the volcanic rock; (**f**) mineral compositions of the granite. Pl: plagioclase; Px: pyroxene; Chl: chlorite; Kfs: potassium feldspar; Bi: biotite; Qtz: quartz.

3. Sample Descriptions

The WDMS grayish-green to dark green volcanic rocks show doleritic texture and vesicular–amygdaloidal structure (Figure 3b). The mineral composition consists of pyroxene (30~40 vol%) and plagioclase (40~60 vol%). Plagioclase occurs as elongate strips with a length of 0.05~1.5 mm and a length–width ratio greater than 3:1. It develops Carlsbad and polysynthetic twinning, and saussuritization is present. Subhedral–anhedral short columnar pyroxene is 0.1~0.5 mm in length and filled between plagioclases. Vesicles and amygdales are well-developed in the rock, with a content of about 10 vol% and a size of 0.1~0.7 mm, and the vesicles are filled chlorite (Figure 3e).

The WDMS grayish-white granite with medium-fine grained granitic texture and massive structure. The mineral composition includes plagioclase (An 25~40) (30~35 vol%), K-feldspar (28~45 vol%), quartz (20~25 vol%), biotite (~5 vol%), and accessory minerals such as apatite, sphene, and metallic minerals. Plagioclase occurs as lath-shaped crystals (~2 mm in length) with polysynthetic twinning and exhibits sericitization. K-feldspar appears as anhedral grains (0.5~2 mm) with grid twinning and have kaolinization alteration. Quartz forms anhedral grains (0.5~1 mm) and the dark mineral biotite occurs as tabular flakes (~0.3 × 0.5 mm) with partial chloritization (Figure 3f).

One volcanic rock was selected for geochronology studies, and one granite sample was used for geochronology and zircon Hf isotope studies. Five volcanic rocks and five granites were used for geochemical studies.

4. Results

4.1. Zircon U-Pb Geochronology Result and Lu-Hf Isotopes

The zircon U-Pb geochronology and in situ Lu-Hf isotope results are listed in Supplementary Tables S1 and S2, respectively.

Twelve zircons from the WDMS volcanic rock are euhedral to subhedral and columnar in shape, with length-to-width ratios of 2:1~3:1. These zircons display inconspicuous concentric oscillation zones (Figure 4a) but have high Th/U ratios (0.38~1.23) (Table S1), indicating a magmatic origin [32]. All twelve analyses yielded similar apparent $^{206}Pb/^{238}U$ ages of 412~403 Ma, with a weighted mean age of 411.5 ± 2.8 Ma (MSWD = 0.43, n = 12) (Figure 4a).

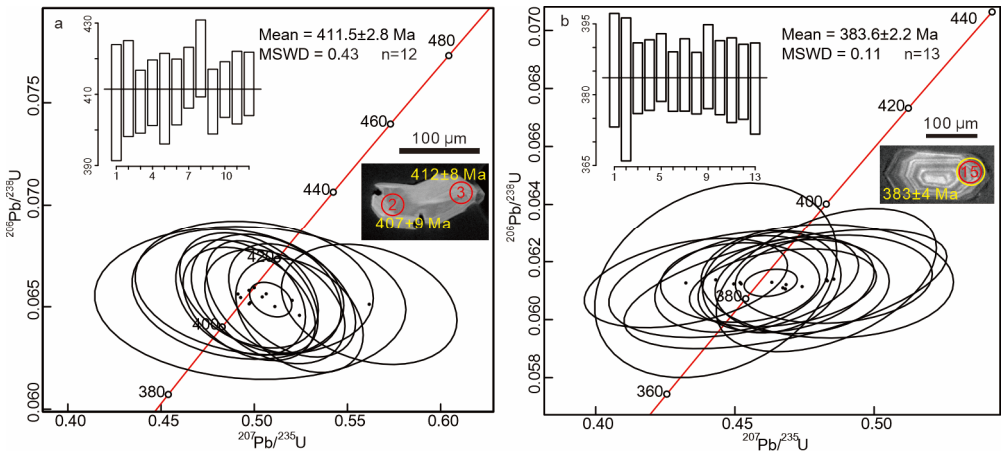


Figure 4. U-Pb concordia diagrams of zircons from Wudaomingshui volcanic rock (**a**) and granite (**b**). Cathodoluminescence images for two zircons from each sample are also shown. Red and yellow circles represent the U-Pb analytical sites and zircon Lu-Hf isotope analysis sites on the Wudaomingshui volcanic rock and granite, respectively.

Thirteen zircon grains from granites were analyzed to determine their U-Pb ages. All these analyzed zircons are euhedral and display granular elongated columnar crystals with length/width ratios of 2:1~3:1 (Figure 4b). Moreover, all these zircons exhibit obvious concentric oscillatory zoning (Figure 4b), and high Th/U ratios (0.25~0.59), indicating a magmatic origin [32]. All these analyses yield close apparent $^{206}Pb/^{238}U$ ages of 382~384 Ma and yield a weighted mean age of 383.6 ± 2.2 Ma (MSWD = 0.11, n = 13) (Figure 4b). Thirteen zircon grains were also analyzed for their Lu-Hf isotopic compositions and exhibited low $^{176}Lu/^{177}Hf$ ratios (0.0017467~0.0026975), and the contribution of ^{176}Hf derived from the decay of ^{176}Hf after zircon crystallization can be considered negligible, and the measured $^{176}Hf/^{177}Hf$ ratios can represent the Hf isotopic composition of the magmatic system from which the zircons crystallized [5]. The zircon Hf isotopic composition of WDMS granites is $^{176}Hf/^{177}Hf$ = 0.282478~0.282642, corresponding to $\varepsilon_{Hf}(t)$ = −2.5~3.3, T_{DM2} = 1310~1013 Ma.

4.2. Whole-Rock Major Oxide and Trace Elements

The major oxide and trace element analysis result are presented in Supplementary Table S3.

4.2.1. Major Oxide

WDMS volcanic rocks underwent alteration, as indicated by high loss on ignition (LOI) ratios (1.15~4.23) and petrological characteristics (Figure 3e). Due to the high mobility of elements such as K and Na during alteration, immobile elements are chosen to assess the alkalinity of samples. Volcanic rock samples have low SiO_2 (47.35~55.59 wt.%) and P_2O_5 (0.18~0.30 wt.%) contents and are plotted in the andesite/basalt-andesite fields (Figure 5a). This characteristic indicates that the WDMS volcanic rocks are basalt-basaltic andesites. Samples also have high contents of TiO_2 (1.46~4.16 wt.%), TFe_2O_3 (2.71~6.87 wt.%) and MgO (3.81~8.29 wt.%) with $Mg^{\#}$ values of 43.95~64.77. The Al_2O_3, Na_2O, and K_2O contents are 13.20~16.45 wt.%, 2.81~5.70 wt.%, and 0.24~1.78 wt.%, respectively, and the contents of Na_2O are higher than those of K_2O (Na_2O/K_2O = 1.58~24.24). Samples are plotted in the calc-alkaline fields in the Ce/Yb vs. Ta/Yb diagram (Figure 5b) and indicate these volcanic rocks are in the same calc-alkaline series as volcanic rocks of the SGJ Formation in the SBOB.

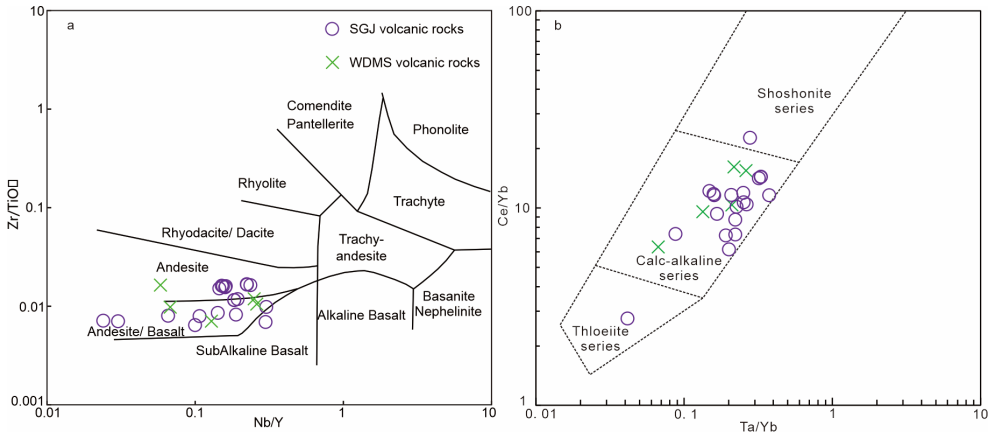


Figure 5. (**a**) Zr/TiO_2 vs. Nb/Y diagram [33]; (**b**) Ce/Yb vs. Ta/Yb diagram [34].

WDMS granite samples have high SiO_2 (65.44~68.86 wt.%) and Na_2O + K_2O (6.64~7.40 wt.%) contents. The Na_2O contents of samples are slightly higher than K_2O contents (Na_2O = 3.46~3.96 wt.%; K_2O = 2.71~3.84 wt.%; Na_2O/K_2O = 0.92~1.45), and samples display high-K calc-alkaline characteristics (Figure 6a). Granites exhibit low TiO_2

(0.32~0.57 wt.%) and P_2O_5 (0.10~0.15 wt.%) contents, high TFe_2O_3 (3.00~4.27 wt.%) and Al_2O_3 (15.51~17.20 wt.%) contents, with A/CNK values of 1.09~1.13, and plotted in the peraluminous field (Figure 6a). Samples also have high MgO contents (1.25~1.68 wt.%) and $Mg^{\#}$ values (34.71~37.75) with low SI consolidation index (9.85~11.80) and high DI differentiation index (70.69~80.45).

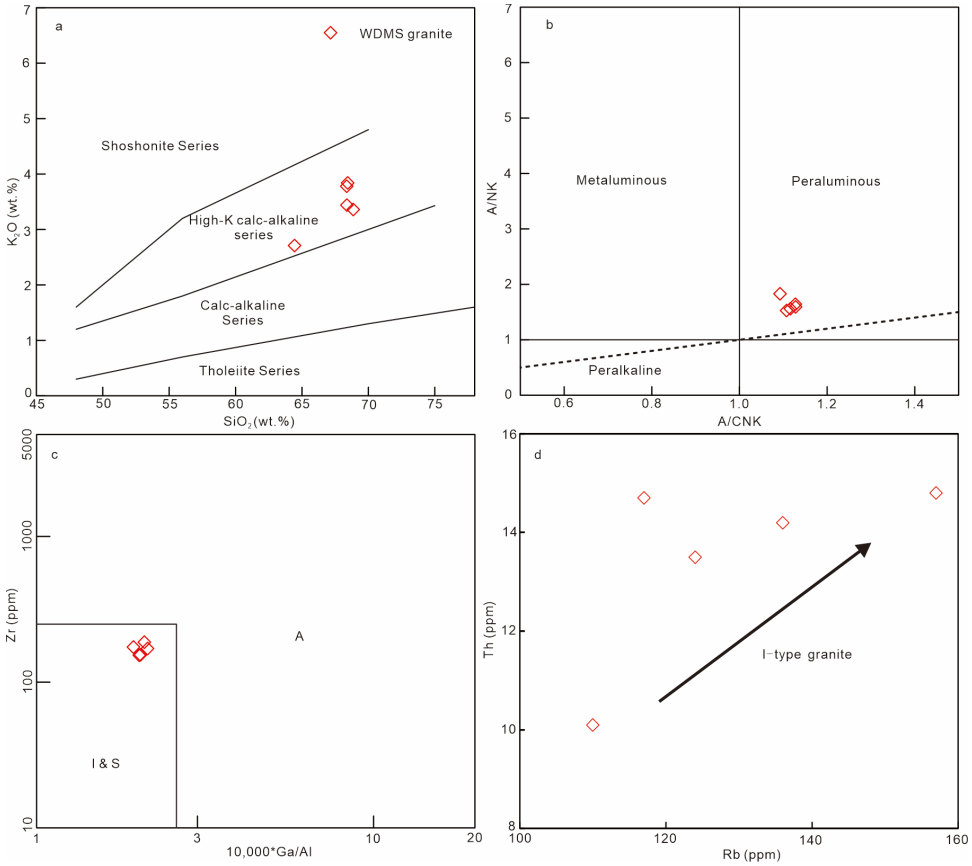


Figure 6. (**a**) K_2O vs. SiO_2 diagram [35]; (**b**) A/NK vs. A/CNK diagram [36]; (**c**) Zr vs. 10,000 *Ga/Al diagram [37]; (**d**) Th vs. Rb diagram.

4.2.2. Trace Elements

The concentration of rare earth elements (REE) in Wudaomingshui volcanic rock samples are 95.10~146.90 ppm. Samples have enrichments of light REEs (LREE) and depletion of heavy REEs (HREE) [$(La/Yb)_N$ = 1.51~5.01; LREE/HREE = 2.55~5.26] and are weakly negative to no Eu anomalies (δEu = 0.84~1.07) (Figure 7a). Samples show positive anomalies in Rb, Ba, Th, and other large ion lithophile elements (LILEs), negative anomalies in Nb, Ta, Ti, and other high-field strength elements (HFSEs) (Figure 7b). In addition, they also have weakly positive anomalies in Zr and Hf (Figure 7b).

The WDMS granites have enrichment of LREEs, depletion of HREEs [$(La/Yb)_N$ = 7.21~9.37, LREE/HREE = 7.41], and with moderate negative Eu anomalies (δEu = 0.52~0.71) (Figure 7a). All granite samples show pronounced positive anomalies in LILEs and negative anomalies in HFSEs (Figure 7b).

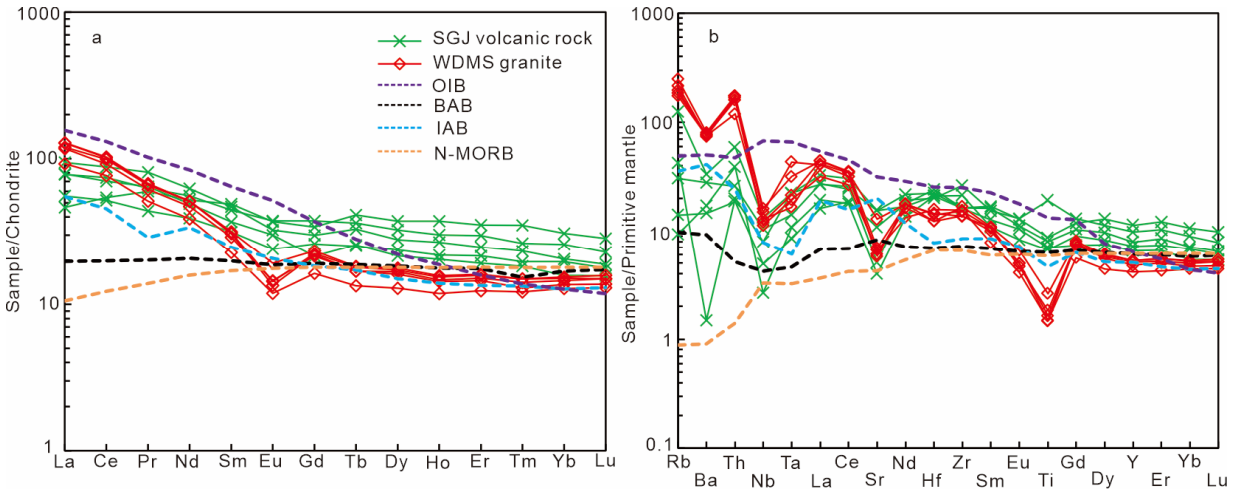


Figure 7. Chondrite-normalized REE diagram (**a**) and primitive-mantle-normalized trace element spider diagram (**b**) for Wudaomingshui volcanic rocks and granites. The values of chondrite and primitive mantle are from Sun and McDonough [38].

5. Discussion

5.1. Petrogenesis

5.1.1. Volcanic Rocks

WDMS volcanic rock samples exhibit elevated Loss on Ignition (LOI) values and pronounced mineral alteration features, indicating substantial post-magmatic alteration. Given the high mobility of incompatible elements such as LILEs, we employed relatively immobile elements, including HSFEs and REEs, to decipher the primary geochemical signatures of the magmatic source.

The Rb/Sr (0.04~0.25) and Lu/Yb (0.13~0.15) ratios of these basalt-basaltic andesites closely overlap with mantle-derived magma ratios (0.06~0.10 and 0.14~0.15, respectively), but distinctly differ from crustal melt signatures (35 and 0.16~0.18) [38,39], supporting a dominant mantle origin. During their ascent through the continental crust, mantle-derived basaltic magmas may undergo variable degrees of fractional crystallization and crustal contamination. Compared to primary basaltic magmas with high $Mg^{\#}$ values (68~75) [40], the WDMS basalt-basaltic andesite samples exhibit moderate MgO contents and Mg# values (except for sample 2013XYQ5-1: MgO = 8.291 wt.%; $Mg^{\#}$ = 64.77), suggesting the influence of fractional crystallization. However, the position correlations of both samples and volcanic rocks of the SGJ Formation in the western segment of the SBOB (Figure 8a) indicate that these rocks have underwent limited fractional crystallization, with partial melting being the dominant process. The WDMS basalt-basaltic andesite samples have low concentrations of Cr (3.7~200.06 ppm) and Ni (1.7~99.3 ppm) compared to these primitive basaltic magmas (Cr > 400 ppm, Ni > 235 ppm) and samples display an olivine fractional crystallization trend in the Ni vs. Nb/Ta diagram (Figure 8b). These characteristics indicate the separation of Mg-Fe-rich minerals (e.g., olivine) during magma evolution.

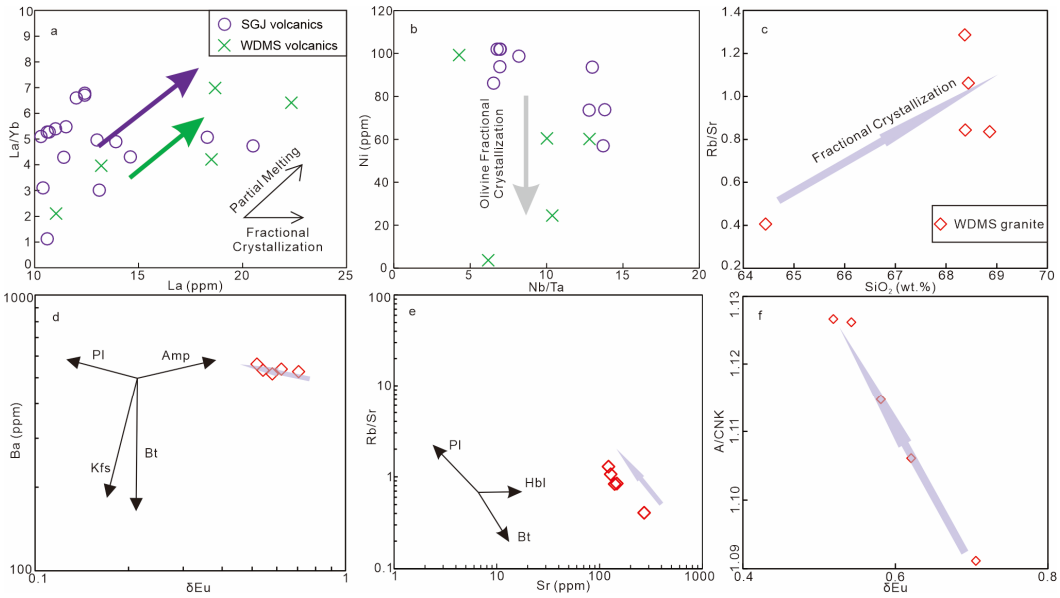


Figure 8. (**a**) La/Yb vs. La diagram [41]; (**b**) Ni vs. Nb/Ta diagram; (**c**) Rb/Sr vs. SiO_2 diagram [42]; (**d**) Ba vs. δEu diagram [5]; (**e**) Ba vs. Rb diagram [5]; (**f**) A/CNK vs. δEu diagram.

Mafic rocks affected by crustal contamination typically exhibit Nb/La < 1 and $(Th/Nb)_{PM}$ > 1 [43]. Basalt-basaltic andesite samples have Nb/La values of 0.14~0.42 and $(Th/Nb)_{PM}$ values of 2.47~14.57. In addition, all samples are plotted within the crustal contamination field (Figure 9a), consistent with the compositional range of the SGJ Formation volcanic rocks in the SBOB, indicating significant crustal input during magma evolution. The $(Th/Yb)_{PM}$ values of samples (1.76~8.32) are between lower crustal (4.6) and upper crustal (28) reference values [44], with closer affinity to the lower crust. Additionally, samples also have Nb/Ta ratios (4.28~12.81) between those indicative of the lower crust (8.3) and mantle (17.39) [38,39]. The above geochemical characteristics suggest that the crustal contamination occurred during the formation of basalt-basaltic andesites (Figure 9b).

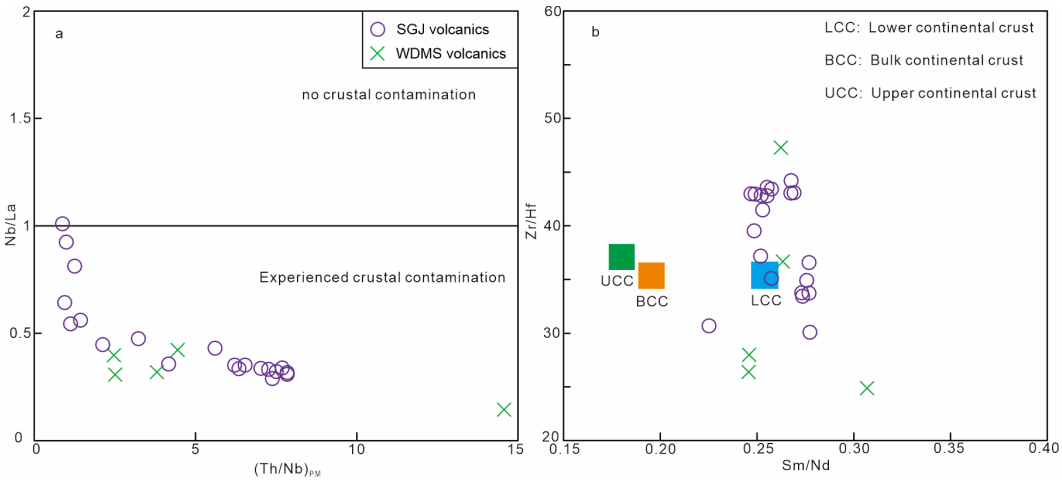


Figure 9. (**a**) Nb/La vs. $(Th/Nb)_{PM}$ diagram [45]; (**b**) Zr/Hf vs. Sm/Nd diagram [46].

The WDMS basalt-basaltic andesite samples have enrichment of LREE and LILE (Figure 7a,b) suggest that they originated from either an enriched asthenosphere or a metasomatized lithosphere modified by subduction-related components [47,48]. Rocks originating from the asthenosphere are typically enriched in LILEs and HFSEs, whereas the

samples are enriched in LILEs and depleted in HFSEs (Figure 7b). Additionally, samples are plotted distinctly away from the Ocean Island Basalt (OIB) (Figure 10a), and rocks also exhibit higher La/Nb (2.37~6.95) and La/Ta (20.07~32.20, avg. 27.61) ratios than values of asthenosphere-derived magmas [38]. Therefore, these geochemical signatures indicate that the parent magma did not originate from the asthenosphere but from the lithosphere. This pattern contrasts sharply with typical asthenosphere-derived magmas and instead points to a subduction-modified lithosphere source. The Nb/La ratios of lithosphere and asthenosphere are <0.4 and >1, respectively [49]. The Nb/La values of samples are 0.14~0.42 (avg. 0.31) consistent with the value of lithosphere. Additionally, their negative δNb values (−1.15 to −0.19) indicate a depleted mantle source. At the same time, samples collectively display an enriched evolutionary trend aligned with the SGJ Formation volcanics in the SBOB (Figure 10a). These geochemical features demonstrate that the WDMS basalt-basaltic andesites originated from a metasomatized and depleted lithosphere enriched by subduction-related components. Subduction materials include subduction fluid and subduction melts. Samples have low Th/La (0.09~0.25), Th/Yb (0.30~1.43), and Th/Ta (1.84~7.43, avg. 4.62) ratios with high Ba/Th (6.12~89.00, avg. 48.33) ratios, which are consistent with values of melts generated by the mantle metasomatized by subduction fluids [50,51]. Melts originating from garnet-facies lherzolite typically exhibit Dy/Yb > 2.5, whereas those from spinel-facies lherzolite yield Dy/Yb < 1.5. Melts derived from a garnet-spinel transitional mantle source show intermediate Dy/Yb values (1.5~2.5) [52,53]. The WDMS volcanic rocks display Dy/Yb ratios of 1.81~2.04, plotting near the spinel-garnet lherzolite partial melting trend (Figure 10b), with an estimated partial melting degree of ~10%. In summary, the WDMS volcanic rocks formed through partial melting of the garnet-spinel transitional lherzolite mantle metasomatized by subduction fluid. Subsequent magma evolution involved olivine-dominated fractional crystallization and assimilation-contamination processes with lower crustal materials.

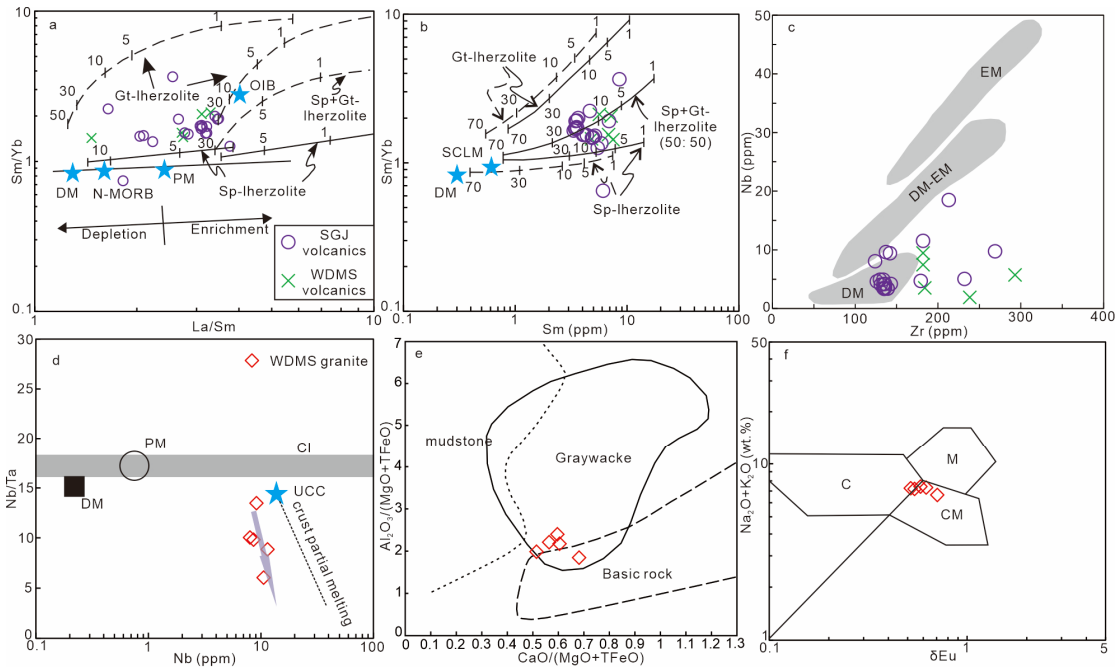


Figure 10. (**a**) Sm/Yb vs. La/Sm diagram [54]; (**b**) Sm/Yb vs. Sm diagram [55]; (**c**) Nb vs. Zr diagram [56]; (**d**) Nb/Ta vs. Nb diagram [56]; (**e**) [Al_2O_3/(MgO + TFeO)] vs. [CaO/(MgO + TFeO)] diagram [57]; (**f**) (Na_2O + K_2O) vs. δEu diagram [58]. PM: primitive mantle; DM: depleted mantle; Sp: spinel; Gt: garnet; EM: enriched mantle; C1: Chondrite; UCC: upper crust; C: crust; M: mantle; CM: crust-mantle mixed source; SCLM: subcontinental lithospheric mantle.

5.1.2. Granites

Granite can be classified as I-, S-, M- and A-type [59–61]. The WDMS granite samples have high K_2O contents (2.71~3.84 wt.%), which is different from the M-type granite with low K_2O contents (<1 wt.%) [62]. Samples exhibit distinct 10,000 × Ga/Al (1.94~2.13), K/Rb (199.87~238.40) and Zr + Nb + Ce + Y (243.90~281.85 ppm) values compared to those of A-type granites [37]. The TFeO/MgO (2.94~3.35) ratios are also different from the iron-enriched signatures (TFeO/MgO > 4.0) of A-type granite [37]. In addition, all samples are plotted within the I- and S-type fields. Therefore, the WDMS granite are I- or S-type. S-type granite is characterized by A/CNK > 1.1, P_2O_5 > 0.2 wt% and enriched in Al-rich phase minerals (e.g., muscovite, garnet) [60,63]. Although samples exhibit weakly peraluminous characteristics (A/CNK = 1.09~1.13), their low P_2O_5 contents (0.10~0.15 wt.%, <0.2 wt.%) and lack of Al-rich minerals in the mineral assemblage distinguish them from S-type granites. In addition, samples have a 10,000 *Ga/Al ratio (2.04) close to that of I-type granite (2.1), and their Th contents increases with the increase in Rb contents (Figure 6c), which indicates that the WDMS granites belong to I-type granite [37].

Notably, samples exhibit low SI consolidation index (9.85~11.80) and high DI differentiation index (70.69~80.45), coupled with a trend in which the Rb/Sr ratios increase with the increasing in SiO_2 contents (Figure 8c). These geochemical trends collectively indicate that the rocks underwent intense fractional crystallization during magmatic evolution. Highly fractionated granites are typically characterized by low ΣREE concentrations, LREE/HREE ratios, K/Rb ratios and TFeO contents (<1 wt%), coupled with strongly negative Eu anomalies [64]. Additionally, they also have elevated Be and significantly reduced Zr concentrations [60]. Granites have high ΣREE concentrations (108.67~145.73 ppm), LREE/HREE ratios (7.46~8.35), K/Rb ratios (199.87~238.40), and TFeO contents (3.68~5.49 wt.%), with weakly negative Eu anomalies, which indicates that samples do not belong to highly fractionated granites. Zr/Hf ratios are critical indicators to determine whether the felsic rocks are highly fractionated granites or not. Highly fractionated granites are characterized by Zr/Hf < 25, while moderately fractionated granites exhibit Zr/Hf values of 25~55 [65,66]. Zr/Hf ratios of samples are 34~49, suggesting the granite underwent moderate fractional crystallization but do not qualify as highly fractionated granitic rocks. Pronounced negative anomalies in Eu, Ba, and Sr (Figure 7) indicate significant plagioclase fractionation (Figure 8d,e). Plagioclase, a major Al-bearing phase, contributes to increasing Al_2O_3 contents and A/CNK values in residual melts during fractionation. Consequently, the strongly peraluminous signatures of the samples (A/CNK = 1.09–1.13) are inferred to have resulted from crystal fractionation-dominated processes rather than pure sedimentary source melting, as demonstrated by the Al_2O_3 vs. A/CNK covariation trend (Figure 8f).

There are three primary genetic mechanisms for I-type granites: (1) crustal anatexis triggered by mantle-derived magma underplating [67]; (2) crust-mantle hybridization [68]; (3) fractional crystallization of mafic magmas [69]. There are limited Silurian-Devonian mafic rocks exposed in the WDMS, and the igneous rocks formed in the Silurian-Devonian are dominated by felsic rocks (Figure 2a). Granites are characterized by high silicon, potassium and total alkali contents, the depletion of Ba, Ti, and Eu, and low Cr-Ni concentrations, indicative of crust-derived magmas [70]. These signatures preclude an origin via fractional crystallization of mafic magmas. The Rb/Sr (0.41~1.29), Ti/Zr (11.13~18.08), and Sm/Nd (0.19~0.20) ratios of the WDMS granites are consistent with crust-derived magma (Rb/Sr > 0.35; Ti/Zr < 20; Sm/Nd < 0.3) [71]. The Nb/Ta ratios (6.02~13.46) and $Mg^{\#}$ values (34.71~37.75) of samples are consistent with melts from the lower crust (Nb/Ta = 8.3~11.4, $Mg^{\#}$ < 45) [71,72], which is supported by samples plotted near the trend in crustal partial melting (Figure 10d). However, the CaO/Na_2O ratios of granite samples are 0.54~0.89, akin to metagreywacke sources (0.3~1.5) [73]. In the A/FM-C/FM diagram (Figure 10e), samples

are plotted within the overlapping field of mafic melts and greywacke-derived partial melts, suggesting contributions from upper crustal materials during petrogenesis. In addition to the obvious characteristics of crust-derived magma, the relatively high Zr/Hf ratios (34~49) and high MgO and Na_2O contents of samples suggest the influence of mantle [71]. Magmas derived from or contaminated by the lithosphere typically exhibit La/Ta > 25 [74]. The La/Ta values of samples are 15.80~41.76 (avg. 28.58), which indicate the involvement of mantle-derived components during petrogenesis (Figure 10f). Zircon Hf isotopes serve as a critical tool for investigating continental crustal growth and evolution [75]. The negative zircon $\varepsilon_{Hf}(t)$ values coupled with T_{DM2} ages significantly exceeding their crystallization ages are evidence that the felsic rocks were derived from partial melting from ancient crust; positive $\varepsilon_{Hf}(t)$ values with T_{DM2} ages approximating crystallization ages, suggesting that the felsic magma originated from the partial melting of juvenile crust (derived from depleted mantle sources) or substantial mantle input during magma generation; widely variable $\varepsilon_{Hf}(t)$ values demonstrate contributions from hybrid sources, reflecting the incorporation of both ancient crustal components and juvenile mantle-derived materials during petrogenesis [75]. Samples exhibit high zircon $\varepsilon_{Hf}(t)$ values (−2.51~+3.32) and Mesoproterozoic T_{DM2} ages (1310~1013 Ma), which closely resemble those of the Mesoproterozoic mafic igneous rocks constituting the basement of the SBOB [7]. These features indicate that monzogranites originated from partial melting of Mesoproterozoic mafic magmatic rocks [7]. Additionally, samples display significant variations in $\varepsilon_{Hf}(t)$ values, plotted between the evolution line for depleted mantle and evolution line for crust extracted from mantle at Ca. 1.0 Ga. This geochemical signature further attests to mantle-derived contributions to the crustal magmas, reflecting hybridization between ancient crustal melts and juvenile mantle-derived components during petrogenesis [7,59].

5.2. Early–Middle Devonian Magmatism in the SBOB

In the Paleozoic stratigraphic sequence of the SBOB, two major unconformity events occurred during the Silurian-Devonian and Carboniferous-Permian, which indicate tectonic regime transitions in these periods [76]. The Devonian is a critical temporal marker for the Silurian-Devonian unconformity. Investigating the magma source and tectonic settings of Devonian igneous rocks holds significant implications for reconstructing the process of accretionary orogenesis and the ocean–continent transition of the PAO at this tectonic junction. The Devonian magmatic events are subdivided into two stages (Early–Middle Devonian and Late Devonian). The Early–Middle Devonian K-feldspar granite, monzogranite, granodiorite, and volcanics of the SGJ Formation are widely distributed in Huitongshan, Shuangfengshan, Shijinpo, Yemaquan, Yemajing, and Dundunshan [5,8,21,26]. Based on zircon U-Pb ages of volcanic rocks and sedimentary rocks within the stratum, combined with geological evidence of unconformable contacts between this formation and both the underlying strata and overlying Late Devonian Dundunshan Formation, the depositional age of the SGJ Formation is 420~390 Ma (Early Devonian) [26,27]. The SGJ Formation in the WDMS were previously assigned to the Silurian Gongpoquan Formation in the 1:200,000 Wudaoming Geological Map. However, the zircon U-Pb age of basalt-basaltic andesite is 411.5 ± 2.8 Ma (MSWD = 0.43), indicating an Early Devonian rather than the Silurian. Meanwhile, the strata of WDMS and the SGJ Formation in the BOB have similar rock assemblage (such as amygdaloidal basalts, trachybasalts, andesites, siltstones, sandstones, mudstones, and siliceous rocks). In terms of geochronology and rock assemblage characteristics, the two are similar. In addition, both of the WDMS basalt-basaltic rocks and mafic rocks of the SGJ Formation in the BOB have similar geochemical compositions and magma source (Figures 8a–c, 9 and 10a–c). Therefore, we suggest that the strata previously assigned to the Silurian Gongpoquan Formation in the WDMS should be reclassified as the Early–Middle

Devonian SGJ Formation. The WDMS granite intrudes into Ordovician quartz diorites and Silurian granodiorites (Figure 2a), indicating a post-Silurian emplacement age. Zircon U-Pb dating of the WDMS granite is 383.6 ± 2.2 Ma (MSWD = 0.11), consistent with field cross-cutting relationships, which constrains its magmatic crystallization to the Middle Devonian. Consequently, the Early Devonian mafic volcanic rocks of the SGJ Formation and Middle Devonian granites in the WDMS collectively represent a tectonic response to the Early–Middle Devonian magmatic events in the SBOB.

5.3. Transition from Advancing to Retreating Accretionary Orogens in the SBOB During the Early–Middle Devonian

Accretionary orogenesis encompasses advancing accretionary orogenesis and retreating accretionary orogenesis, which reflect contrasting plate tectonic dynamics and exhibit markedly divergent geological characteristics [77]. In advancing accretionary orogenesis, sustained compressional advancement of the subducting slab against the overriding plate drives vertical crustal thickening and horizontal shortening. This process is dominated by convergent dynamics, generating igneous rocks exhibiting diagnostic subduction-related geochemical signatures. In contrast, retreating accretionary orogenesis features sustained slab rollback of the descending plate, leading to extensional thinning of the overriding plate. This results in vertical crustal thinning and lateral extension, manifesting as rock assemblages formed in the extensional setting accompanied by extensional structures [77]. The Early–Middle Devonian magmatic rocks in the SBOB comprises not only A-type granites, within-plate basalts (WPB), and highly fractionated I/S-type granites which formed in the extensional setting but also adakites and Nb-enriched basalts were also formed in the SBOB [19–22,30]. This juxtaposition of comparative rock assemblages has sparked ongoing debates regarding the tectonic setting and geodynamic processes governing the SBOB during the Early–Middle Devonian [7,8,21,27]. WDMS mafic rocks have the characteristics of both WPB [high TiO_2 and Zr contents, weakly enriched in Zr and Hf, Zr/Y > 3 (4~7), Th/Nb > 0.11 (0.29~1.74), Th/Ta > 1.6 (1.84~7.43); Figure 11a] and arc basalt [enriched in LILEs, depleted in HFSEs (Nb, Ta), high Al_2O_3 contents (13.20~16.45 wt.%) and low Nb and Ta concentration; Figure 11b] [47,78]. Granites exhibit relatively low Sr concentration (122~271 ppm) and Sr/Y ratios (5.54~11.29), indicating a thinner crustal thickness. However, the Th/Ta and Y/Nb ratios (8.07~18.38 and 1.90~2.79, respectively), which are greater than 6 and 1.2, display characteristics typical of subduction zone granites. Although the contemporaneous formation of these contrasting geochemical signatures and rock assemblages formed in diverse environments poses challenges for determining the Early–Middle Devonian tectonic setting of the SBOB, these features also provide critical constraints for investigating the transition from advancing to retreating accretionary orogenesis in this region. We proposed that the WDMS basalt-basaltic andesites and granites exhibit dual geochemical affinities to both extensional and subduction-related magmatism, and the co-occurrence of A-type granite, WPB, adakite, and Nb-rich basalt formed in Devonian is interpreted to indicate a transition from advancing to retreating accretionary orogenesis at this time. The rationale for this interpretation is as follows: (1) In advancing accretionary orogens, crustal recycling dominates, whereas retreating accretionary orogen are characterized by substantial addition of juvenile material [79]. The WDMS granite originated from partial melting of the basaltic lower crust, and is influenced by mantle-derived magma, which indicates the addition of juvenile material during petrogenesis. Statistical analysis of Hf isotopes for all Devonian felsic rocks in the SBOB reveals that their $\varepsilon_{Hf}(t)$ values generally exhibit a decline evolutionary trend during 420~380 Ma, followed by a subsequent increase during 380~360 Ma (Figure 12). This evolution trend reflects a transition from lateral arc accretion dominated by subduction-driven processes to vertical inputs of mantle-derived materials. Furthermore, the presence of highly variable zircon $\varepsilon_{Hf}(t)$ values

in pre-Devonian magmatic rocks, coupled with the predominantly positive $\varepsilon_{Hf}(t)$ values in later magmatic zircons, provides evidence for substantial juvenile material input during Early–Middle Devonian magmatism in the SBOB. (2) Early Paleozoic Basaltic rocks in the SBOB with tholeiitic and that are Nb-enriched are interpreted to originate from partial melting of the mantle wedge. At same times, the intermediate to felsic rocks dominantly comprise calc-alkaline I-type granitoids, while adakites have high Sr and low Y concentrations identified in the SH unit. These features collectively indicate that the SBOB resided in a subduction-related arc setting during the early Paleozoic [19,20]. However, A-type felsic rocks and mafic rocks have high Zr, TiO_2 contents and Zr/Y ratios, which indicates that an intraplate extensional environment emerged in the SBOB beginning in the Early Devonian [7,8,26], as well as bimodal volcanic rocks also reported in the Yemaquan area of the SBOB [27]. There is variation in the geochemical characteristics and rock assemblages of igneous rocks that formed in early Paleozoic to Devonian reflecting a tectonic transition, that is, the regional transformation from subduction convergence to an extensional tectonic setting. As for basalt-basaltic andesites and granites in this study, although all of them have geochemical characteristics of arc magmatic rocks, volcanic rocks show more obvious geochemical characteristics of WPB [such as Zr/Y > 3 (4~7), Th/Nb > 0.11 (0.29~1.74), Th/Ta > 1.6 (1.84~7.43)] (Figure 11a). Granite samples are plotted in the post-orogenic granite field (Figure 11c) with low Sr/Y (5.54~11.29) and La/Yb (10.05~13.06) ratios, reflecting the shallow melting of magma source. At same time, basalt-basaltic andesites and granites are plotted in the transition zone of arc and extensional magmatic rocks (Figure 11b,d), which also reflects the tectonic transition from advancing to retreating accretionary orogenesis; (3) In addition to the distribution of A-type granites in the Early Devonian, S-type granites are also distributed in this area [80]. These S-type granites have similar characteristics to the Permian S-type granites in New England, and these S-type granites in New England record the transition of the Terra Australis orogenic belt from the convergent to the extensional tectonic setting [81].

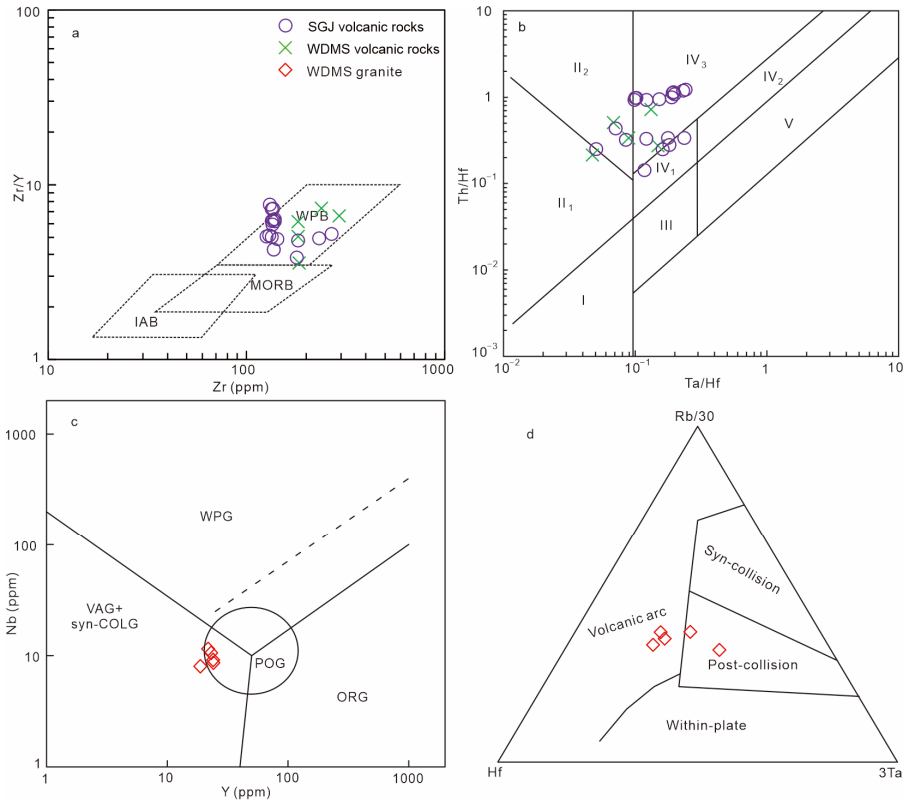


Figure 11. (**a**) Zr/Y vs. Zr diagram [82]; (**b**) Th/Hf vs. Ta/Hf diagram [78]; (**c**) Nb vs. Y diagram [83]; (**d**) Rb/30 vs. Hf vs. 3Ta diagram [84]. MORB: mid-ocean ridge basalt; IAB: island-arc basalt;

WPB: within-plate basalt; VAG: volcanic arc granite; POG: post-orogenic granite; ORG: ocean ridge granite; WPG: within-plate granite; syn-COLG: syn-collisional granite; I: divergent boundary; II: Convergent boundary: II_1: Ocean island arc basalt; II_2: Continental arc basalt; III: Ocean island basalt, Seamount basalt, T-MORB and E- MORB; IV. Continental within-plate basalt: IV_1: Tholeiitic basalts in continental rifts and continental margins; IV_2: Alkali basalts in continental rifts; IV_3: Basalts in continental extensional zones (or incipient rifts); V. Mantle plume-related tholeiitic basalts or N-MORB. The dashed line represents the upper compositional boundary for ORG from anomalous ridge segments.

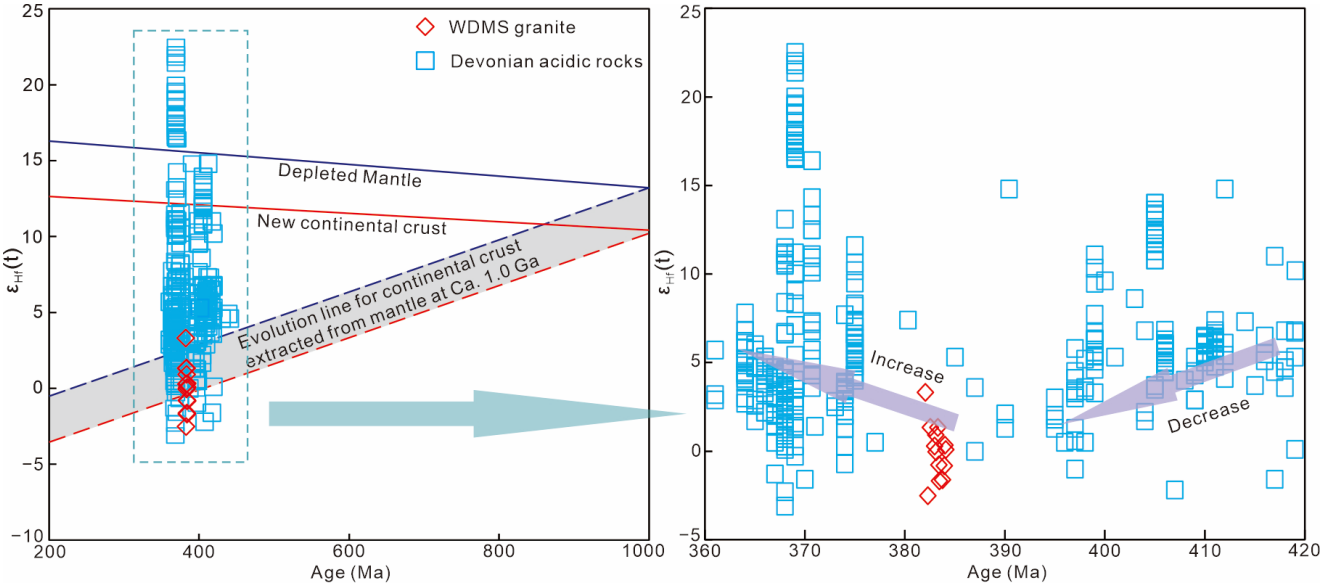


Figure 12. $\varepsilon_{Hf}(t)$-Age diagram of the WDMS granite and Devonian acidic rocks from the SBOB [7]. Ages and $\varepsilon_{Hf}(t)$ values of Devonian acidic rocks from [5,8,18–21,23–27].

From a sedimentological perspective, the Early Paleozoic strata in the SBOB are predominantly composed of pyroclastic rocks, limestones, sandstones, and mudstones, deposited in upper bathyal to neritic environments [85]. A large-scale unconformity separates the Late Paleozoic from the Early Paleozoic successions. The Middle-Lower Devonian SGJ Formation constitutes a molasse-type deposit, showing the characteristics of rapid accumulation [76,86]. Its vertical grain-size profile shows a vertical sequence of coarse–fine–coarse, and the depositional systems transition from subaqueous fan deposits, through fluvial-lacustrine facies to alluvial fan conglomerates. The color variations in sedimentary sequences progressing from reddish-green→green→gray→red collectively record a shallowing–deepening–shallowing cycle of the depositional water column [86]. The late Devonian Dundunshan Formation which in unconformity contact with the SGJ Formation is a continental volcanic sedimentary formation, composed of magmatic rocks (such as rhyolite, rhyolite dacite, andesite) and volcanic clastic rocks (e.g., tuff, volcanic breccia) [18]. The above evidence indicates that the SBOB showed a transition from upper bathyal-neritic facies to littoral-continental facies in the early Paleozoic-Devonian. In addition, magmatic rocks and sedimentary rocks formed in the SBOB during the early Paleozoic have generally suffered deformation and metamorphism, such as the strong mylonitization of granite, indicating that the strong dynamic metamorphism occurred in the region after the formation of these rocks [25]. While the Devonian magmatic rocks and sedimentary rocks did not undergo obvious deformation and metamorphism [87], it is indicated that the strong dynamic metamorphism did not occur in the region after the formation of these rocks, showing that there was a large-scale tectonic event in the SBOB at the turn of the early and

late Paleozoic, and that the transformation of the tectonic system occurred in the region. Characteristics of the sedimentary, deformation, and metamorphism, combined with the diversity of geochemical types and rock assemblages of the Early–Middle Devonian magmatic rocks in the SBOB, support the view that the transition from advancing to retreating accretionary orogenesis in the SBOB during the Early-Mid Devonian.

The core of the transformation of the accretionary orogenic shape is the process that the underlying plate push the overlying plate transform into the process that the underlying plate retreats and leads to the extension and thinning of the overlying plate. The HNXOB and HZOB are located on the north and south sides of the SH unit (Figure 1b). A critical question arises: which of these two ophiolite belts represents the subducting slab that acted as the underlying plate driving the accretionary orogenic regime transition during this tectonic transformation? The zircon U-Pb ages of gabbro and oceanic plagiogranite in the Hongliuhe-Niujuanzi-Xichangjing ophiolite range from 508~536 Ma, indicating an Early–Middle Cambrian formation age [7,88]. It is the product of the north–south bidirectional subduction and closure of the Hongliuhe-Niujuanzi-Xichangjing paleo-ocean basin [18]. The subduction process continued until the Silurian. Affected by this process, a series of arc magmatic rocks were produced on the SH unit [19,20], and the back-arc basin represented by the HZOB was formed by extension on the south side of the tectonic unit at 444.9 ± 2.1 Ma [18]. The tectonic evolution of the SBOB is affected by the subduction of the Hongliuhe-Niujuanzi-Xichangjing paleo-ocean basin. The Early Devonian A-type granite is the earliest A-type granite in the Beishan orogenic belt. It is widely distributed in the Mazongshan unit and SH unit on both sides of the HBOB, which corresponds to the early–late Paleozoic tectonic regime transformation event in the BOB. At the same time, the Hongliuhe hornblende gabbro and Zhaobishannan A-type granite with the characteristics of within-plate basalt formed at 404 Ma and 408 Ma intruded into the Hongliuhe ophiolite as a nailed rock mass [18], indicating that the Hongliuhe-Niujuanzi-Xichangjing paleo-ocean basin was closed before the Early Devonian. Therefore, the Hongliuhe-Niujuanzi-Xichangjing paleo-ocean basin experienced continuous compressional convergence with the SH unit, without exhibiting extension in the overlying plate caused by retreat of the underlying slab during Early–Middle Cambrian to pre-Early Devonian. Consequently, we propose that the Huitongshan-Zhangfangshan back-arc basin corresponds to the underlying slab during the transition in tectonic system. Zircon U-Pb dating of gabbro from the Huitongshan-Zhangfangshan ophiolite yields crystallization ages of 446~363 Ma [89–91], with the Zhangfangshan ophiolite (363 Ma) exhibiting characteristics of mafic magmatic rocks formed during the back-arc basin spreading stage, indicating that the Huitongshan-Zhangfangshan back-arc basin remained unclosed until the late Devonian [18]. Simultaneously, Devonian arc magmatic rocks (e.g., adakitic rocks) in southern Beishan are predominantly distributed near the Huitongshan-Zhangfangshan ophiolite belt (e.g., Liuyuan and Heishantou areas) [19,24]. In contrast, the SH unit exhibits an increased proportion of magmatic rocks formed in an extensional tectonic setting distal to this HZOB. In summary, we propose that the underlying slab responsible for the Early–Middle Devonian accretionary orogenic transition in the southern Beishan belt corresponds to the Huitongshan-Zhangfangshan back-arc basin. Specifically, the subduction of this back-arc basin beneath the SH unit transitioned from advancing compression to slab retreat during the Early–Middle Devonian, ultimately driving the tectonic shift from progressive advancing to retreating accretionary orogeny in the SBOB.

6. Conclusions

1. The crystallization age of volcanic rock from Wudaomingshui is 411.5 ± 2.8 Ma (MSWD = 0.43, n = 12), and the granite has crystallization age of 383.6 ± 2.2 Ma (MSWD = 0.11, n = 13). The $\varepsilon_{Hf}(t)$ values of granites are −2.5 to 3.3 with T_{DM2} ages from 1310 to 1013 Ma.
2. The Wudaomingshui volcanics are calc-alkaline basalt-basaltic andesite with low SiO_2 contents (47.35~55.59 wt.%), generated from the partial melting of the depleted lithosphere metasomatized by subduction fluid and contaminated by the lower crust. Granites are high-K calc-alkaline I-type felsic rocks, originating from the partial melting of the lower crust, and influenced by the mantle. The upper crust also affected the formation of granite.
3. Wudaomingshui volcanic rocks and granites were formed in the tectonic switching process from advancing to retreating subduction. Combined with the regional geological background, these findings indicate that the transformation from advancing to retreating accretionary orogenesis occurred in the southern Beishan Orogenic Belt during the Early–Middle Devonian.

Supplementary Materials: The following supporting information can be downloaded at: https://www.mdpi.com/article/10.3390/min15060632/s1, Text S1: Analytical methods for zircon U-Pb geochronology, in situ Lu-Hf isotope analysis and whole-rock geochemistry analysis of the Wudaomingshui volcanic rocks and granites; Table S1: Results of U-Pb dating by zircons from the Wudaomingshui volcanic rocks and granites; Table S2: Zircon Lu-Hf isotope analysis of the Wudaomingshui granites; Table S3: Whole-rock major (wt.%) and trace element (ppm) analyses of the Wudaomingshui volcanic rocks and granites [92–104].

Author Contributions: Methodology, T.H., Y.W. and L.W.; Investigation, J.Y., Z.Y., K.L., Z.W. and T.H.; Resources, T.H.; Data curation, T.H., Z.L., Z.W., K.L. and L.W.; Writing—original draft, T.H. and L.W.; Writing—review and editing, T.H., L.W. and Y.W.; Project administration, T.H. and Y.W.; Funding acquisition, T.H. and Y.W. All authors have read and agreed to the published version of the manuscript.

Funding: This research was supported by Gansu Province Key Research and Development Plan—Industrial Projects (No. 24YFGA015, 22YF7GA050), the projects of Ministry of Natural Resources, a new round of Mineral Exploration Breakthrough Strategic Action Science and Technology Support Projects (No. ZKKJ202410, ZKKJ202427) and Gansu Provincial Federation of Trade Unions employee subsidy fund project Study on mineralization and prospecting of porphyry copper and gold deposits in the western part of North Qilian (202411).

Data Availability Statement: The original contributions presented in the study are included in the Supplementary Material.

Acknowledgments: We would like to thank Wei Xu and Xinwei Zhai for their advance with this manuscript. We sincerely thank the editors and all reviewers for their valuable feedback that we have used to improve the quality of our manuscript.

Conflicts of Interest: The authors declare no conflicts of interest.

References

1. Şengör, A.M.C.; Natal'In, B.A.; Burtman, V.S. Evolution of the Altaid Tectonic Collage and Palaeozoic Crustal Growth in Eurasia. *Nature* **1993**, *364*, 299–307. [CrossRef]
2. Şengör, A.M.C.; Sunal, G.; Natal'in, B.A.; Voo, R.V.D. The Altaids: A review of twenty-five years of knowledge accumulation. *Earth-Sci. Rev.* **2022**, *228*, 104013. [CrossRef]
3. Windley, B.F.; Alexeiev, D.; Xiao, W.J.; Kroöner, A.; Badarch, G. Tectonic Models for Accretion of the Central Asian Orogenic Belt. *J. Geol. Soc.* **2007**, *164*, 31–47. [CrossRef]

4. Xiao, W.J.; Windley, B.F.; Han, C.M.; Liu, W.; Wan, B.; Zhang, J.E.; Ao, S.J.; Zhang, Z.Y.; Song, D.F. Late Paleozoic to Early Triassic Multiple Roll-Back and oroclinal Bending of the Mongolia Collage in Central Asia. *Earth-Sci. Rev.* **2018**, *186*, 94–128. [CrossRef]
5. Xu, W.; Xu, X.Y.; Lu, J.C.; Niu, Y.Z.; Chen, G.C.; Shi, J.Z.; Dang, B.; Song, B.; Zhang, Y.X.; Zhang, Q. Geochronology, Petrogenesis and Tectonic Implications of Devonian High-K Acid Magmatic Rocks from Yemajing Area in Beishan Orogen. *Earth Sci.* **2019**, *44*, 2775–2793. (In Chinese with English abstract)
6. Zhao, G.C.; Wang, Y.J.; Huang, B.C.; Dong, Y.P.; Li, S.Z.; Zhang, G.W.; Li, S. Geological reconstructions of the East Asian blocks: From the breakup of Rodinia to the assembly of Pangea. *Earth-Sci. Rev.* **2018**, *186*, 262–286. [CrossRef]
7. Zheng, R.G.; Zheng, J.Y.; Xiao, W.J.; Zhang, J. Long-lived subduction retreating led to continental rifting along the northern Gondwana: Insights from Devonian igneous rocks and ophiolite in the Beishan orogenic collage. *Lithos* **2023**, *454*, 107236. [CrossRef]
8. Zhu, J.; Lv, X.B.; Peng, S.G. U-Pb zircon geochronology, geochemistry and tectonic implications of the early Devonian granitoids in the Liuyuan area, Beishan, NW China. *Geosci. J.* **2016**, *20*, 609–625. [CrossRef]
9. Saktura, W.M.; Buckman, S.; Nutman, A.P.; Belousova, E.A.; Yan, Z.; Aitchison, J.C. Continental origin of the Gubaoquan eclogite and implications for evolution of the Beishan Orogen, Central Asian Orogenic Belt, NW China. *Lithos* **2017**, *294*, 20–38. [CrossRef]
10. He, Z.Y.; Zhang, Z.M.; Zong, K.Q.; Hua, X.; Klemd, R. Metamorphic P–T–t evolution of mafic HP granulites in the northeastern segment of the Tarim Craton (Dunhuang block): Evidence for early Paleozoic continental subduction. *Lithos* **2014**, *196*, 1–13. [CrossRef]
11. Wu, L.; Zhai, X.; Wang, E.; Chen, W.; Song, G.; Zheng, F.; Zhao, J.; Wang, J.; Wang, H. Early Permian Post-Collision Extensional Setting in the Southern Beishan Orogenic Belt: Evidence from the Zhangfangshan Granodiorite and the Baishantang Bimodal Volcanic Rocks. *Minerals* **2023**, *13*, 1468. [CrossRef]
12. Jahn, B.M.; Wu, F.Y.; Chen, B. Granitoids of the Central Asian Orogenic Belt and continental growth in the Phanerozoic. *Trans.—R. Soc. Edinb.* **2000**, *91*, 181–194.
13. Xiao, W.J.; Windley, B.F.; Sun, S.; Li, J.L.; Huang, B.C.; Han, C.M.; Yuan, C.; Sun, M.; Chen, H.L. A Tale of Amalgamation of Three Permo−Triassic Collage Systems in Central Asia: Oroclines, Sutures, and Terminal Accretion. *Annu. Rev. Earth Planet. Sci.* **2015**, *43*, 477–507. [CrossRef]
14. Huang, B.T.; Wang, G.Q.; Li, X.M.; Bu, T.; Dong, Z.C.; Zhu, T. Precambrian tectonic affinity of the Beishan Orogenic Belt: Constraints from Proterozoic metasedimentary rocks. *Precambrian Res.* **2022**, *376*, 106686. [CrossRef]
15. Song, D.F.; Xiao, W.J.; Zeng, H.; Mao, Q.G.; Ao, S.J. Accretionary orogenic processes of the Beishan orogenic belt. *Geol. Bull. China* **2024**, *43*, 2131–2150. (In Chinese with English abstract)
16. Xiao, W.J.; Mao, Q.G.; Windley, B.F.; Han, C.M.; Qu, J.F.; Zhang, J.E.; Ao, S.J.; Guo, Q.Q.; Cleven, N.R.; Lin, S.F.; et al. Paleozoic multiple accretionary and collisional processes of the Beishan orogenic collage. *Am. J. Sci.* **2010**, *310*, 1553–1594. [CrossRef]
17. Mao, Q.G.; Xiao, W.J.; Windley, B.F.; Han, C.M.; Qu, J.F.; Ao, S.J.; Zhang, J.E.; Guo, Q.Q. The Liuyuan complex in the Beishan, NW China: A Carboniferous-Permian ophiolitic fore-arc sliver in the southern Altaids. *Geol. Mag.* **2011**, *149*, 483–506. [CrossRef]
18. Wu, L. Paleo-Oceanic Basin Convergence Process in the Southern Margin of the Middle Central Asian Orogenic Belt: Petrogeochemical and Geochronological Evidence. Doctoral Dissertation, Lanzhou University, Lanzhou, China, 2024. (In Chinese with English abstract).
19. Mao, Q.G.; Xiao, W.J.; Fang, T.H.; Wang, J.B.; Han, C.M.; Sun, M.; Yuan, C. Late Ordovician to early Devonian adakites and Nb-enriched basalts in the Liuyuan area, Beishan, NW China: Implications for early Paleozoic slab–melting and crustal growth in the southern Altaids. *Gondwana Res.* **2012**, *22*, 534–553. [CrossRef]
20. Ao, S.J.; Xiao, W.J.; Han, C.M.; Li, X.H.; Qu, J.F.; Zhang, J.E.; Guo, Q.Q.; Tian, Z.H. Cambrian to early Silurian ophiolite and accretionary processes in the Beishan collage, NW China: Implications for the architecture of the Southern Altaids. *Geol. Mag.* **2012**, *149*, 606–625. [CrossRef]
21. Li, S.; Wang, T.; Tong, Y.; Hong, D.W.; Ouyang, Z.X. Identification of the Early Devonian Shuangfengshan A-type granitesin Liuyuan area of Beishan and its implications to tectonic evolution. *Acta Petrol. Mineral.* **2009**, *28*, 407–422. (In Chinese with English abstract)
22. Guo, Q.Q.; Xiao, W.J.; Hou, Q.L.; Windley, B.F.; Han, C.M.; Yian, Z.H.; Song, D.F. Construction of Late Devonian Dundunshan arc in the Beishan orogen and its implication for tectonics of southern Central Asian Orogenic Belt. *Lithos* **2014**, *184*, 361–378. [CrossRef]
23. Wang, E.; Zhai, X.; Chen, W.; Wu, L.; Song, G.; Wang, Y.; Guo, Z.; Zhao, J.; Wang, J. Late Devonian A-Type Granites from the Beishan, Southern Central Asia Orogenic Belt: Implications for Closure of the Paleo-Asia Ocean. *Minerals* **2023**, *13*, 565. [CrossRef]
24. Yang, Z.X.; Ding, S.H.; Zhang, J.; Fan, X.X.; Kong, W.Q.; Zhao, J.C.; Jing, D.L. The discovery of Early Devonian adakites in Beishan orogenic belt and its geological significance. *Acta Petrol. Mineral.* **2021**, *40*, 185–201. (In Chinese with English abstract)
25. Song, D.F.; Xiao, W.J.; Han, C.M.; Li, J.L.; Qu, J.F.; Guo, Q.Q.; Lin, L.N.; Wang, Z.M. Progressive accretionary tectonics of the Beishan orogenic collage, southern Altaids: Insights from zircon U-Pb and Hf isotopic data of high-grade complexes. *Precambrian Res.* **2013**, *227*, 368–388. [CrossRef]

26. Cheng, X.Y.; Teng, X.J.; Tian, J.; Duan, X.L. Geochemical characteristics, isotopic ages and tectonic environment of Sangejing Formation in Beishan orogenic belt, Inner Mongolia. *Geol. Bull. China* **2020**, *39*, 1461–1473. (In Chinese with English abstract)
27. Tao, G.H.; Li, X.F.; Chen, W.L.; Chen, W.; Lu, G.; Hao, C.; Pan, S.; Wu, K.N. The geochemical characteristics and tectonic significance of Devonian bimodal volcanic rocks in Yemaquan area of Beishan, Inner Mongolia. *Geol. Bull. China* **2022**, *41*, 1783–1797. (In Chinese with English abstract)
28. Ao, S.J.; Xiao, W.J.; Windley, B.F.; Mao, Q.G.; Han, C.M.; Zhang, J.E.; Yang, L.K.; Geng, J.Z. Paleozoic accretionary orogenesis in the eastern Beishan orogen: Constraints from zircon U-Pb and 40Ar/39Ar geochronology. *Gondwana Res.* **2015**, *30*, 224–235. [CrossRef]
29. He, Z.Y.; Klemdb, R.; Yana, L.L.; Zhang, Z.M. The origin and crustal evolution of microcontinents in the Beishan orogen of the southern Central Asian Orogenic Belt. *Earth-Sci. Rev.* **2018**, *185*, 1–14. [CrossRef]
30. Guo, Q.Q.; Chung, S.L.; Xiao, W.J.; Hou, Q.L.; Li, S. Petrogenesis and tectonic implications of late Devonian arc volcanic rocks in southern Beishan orogen, NW China: Geochemical and Nd–Sr–Hf isotopic constraints. *Lithos* **2017**, *278*, 84–96. [CrossRef]
31. Xie, W.; Song, X.Y.; Deng, Y.F.; Wang, Y.S.; Ba, D.H.; Zheng, W.Q.; Li, X.B. Geochemistry and petrogenetic implications of a Late Devonian mafic–ultramafic intrusion at the southern margin of the Central Asian Orogenic Belt. *Lithos* **2012**, *144*, 209–230. [CrossRef]
32. Hoskin, P.W.O.; Black, L.P. Metamorphic zircon formation by solid-state recrystallization of protolith igneous zircon. *J. Metamorph. Geol.* **2000**, *18*, 423–439. [CrossRef]
33. Winchester, J.A.; Floyd, P.A. Geochemical discrimination of different magma series and their differentiation products using immobile elements. *Chem. Geol.* **1977**, *20*, 325–343. [CrossRef]
34. Pearce, J.A. Trace Element Characteristics of Lavas from Destructive Plate Boundaries. In *Andesites: Orogenic Andesites and Related Rocks*; Thorpe, R.S., Ed.; Wiley: Hoboken, NJ, USA, 1982; pp. 528–548.
35. Whiteford, D.G.; Nicholls, I.A.; Taylor, S.R. Spatial variations in the geochemistry of quaternary lavas across the Sunda arc in Java and Bali. *Contrib. Mineral. Petrol.* **1979**, *70*, 341–356. [CrossRef]
36. Maniar, P.D.; Piccoli, P.M. Tectonic discrimination of granitoids. *Geol. Soc. Am. Bull.* **1989**, *101*, 35–643. [CrossRef]
37. Whalen, J.B.; Currie, K.L.; Chappell, B.W. A-type granites: Geochemical characteristics, discrimination and petrogenesis. *Contrib. Mineral. Petrol.* **1987**, *95*, 407–419. [CrossRef]
38. Sun, S.S.; McDonough, W. Chemical and isotopic systematics of oceanic basalts: Implications for mantle composition and processes. *Geol. Soc. Lond. Spec. Publ.* **1989**, *42*, 313–345. [CrossRef]
39. Hofmann, P.F. United Plates of America, the birth of a craton: Early Proterozoic assembly and growth of Laurentia. *Annu. Rev. Earth Planet. Sci.* **1988**, *16*, 543–603. [CrossRef]
40. Langmuir, C.H.; Bender, J.F.; Bence, A.E.; Hanson, G.N.; Taylor, S.R. Petrogenesis of basalts from the famous area: Mid-Atlantic ridge. *Earth Planet. Sci. Lett.* **1977**, *36*, 133–156. [CrossRef]
41. Dostal, J.; Owen, J.V. Cretaceous alkaline lamprophyres from northeastern Czech Republic: Geochemistry and petrogenesis. *Geol. Rundsch.* **1998**, *87*, 67–77. [CrossRef]
42. Raeisi, D.; Gholoizade, K.; Nayebi, N.; Babazadeh, S. Geochemistry and mineral composition of lamprophyre dikes, central Iran: Implications for petrogenesis and mantle evolution. *J. Earth Syst. Sci.* **2019**, *128*, 74. [CrossRef]
43. Qi, L.; Zhou, M.F. Platinum-group elemental and Sr-Nd-Os isotopic geochemistry of Permian Emeishan flood basalts in Guizhou Province, SW China. *Chem. Geol.* **2008**, *248*, 83–103. [CrossRef]
44. Wang, C.Y.; Zhou, M.F.; Keays, R.R. Geochemical constraints on the origin of the Permian Baimazhai mafic–ultramafic intrusion, SW China. *Contrib. Mineral. Petrol.* **2006**, *152*, 309–321. [CrossRef]
45. Li, T.; Liu, L.; Liao, X.Y.; Gai, Y.S.; Ma, T.; Wang, C. Geochemistry, Sr-Nd-Pb Isotopic Compositions and Zircon U-Pb Geochronology of Neoproterozoic Mafic Dyke in the Douling Complex, South Qinling Belt, China. *J. Earth Sci.* **2020**, *31*, 237–248. [CrossRef]
46. Stefan, W.; Carsten, M.; Klaus, M. Nb/Ta, Zr/Hf and REE in the depleted mantle: Implications for the differentiation history of the crust–mantle system. *Earth Planet. Sci. Lett.* **2003**, *205*, 309–324.
47. Pearce, J.A.; Peate, D.W. Tectonic implications of the composition of volcanic arc magmas. *Annu. Rev. Earth Planet. Sci.* **1995**, *23*, 251–285. [CrossRef]
48. Pearce, J.A. Geochemical finger printing of oceanic basalts with applications to ophiolite classification and the search for Archean oceanic crust. *Lithos* **2008**, *100*, 14–48. [CrossRef]
49. Xia, L.Q.; Li, X.M. Basalt geochemistry as a diagnostic indicator of tectonic setting. *Gondwana Res.* **2019**, *64*, 43–67. [CrossRef]
50. Woodhead, J.D.; Hergt, J.M.; Davidson, J.P.; Eggins, S.M. Hafnium isotope evidence for 'conservative' element mobility during subduction zone processes. *Earth Planet. Sci. Lett.* **2001**, *192*, 331–346. [CrossRef]
51. Jeremy, P.; Richard, S.; Robert, K. Special Paper: Adakite-Like Rocks: Their Diverse Origins and Questionable Role in Metallogenesis. *Econ. Geol. Bull. Soc. Econ. Geol.* **2007**, *102*, 537–576.
52. McKenzie, D.; O'Nions, R.K. Partial Melt Distributions from Inversion of Rare Earth Element Concentrations. *J. Petrol.* **1991**, *32*, 1021–1091. [CrossRef]

53. Aldanmaz, E.; Pearce, J.A.; Thirlwall, M.F.; Mitchell, J.G. Petrogenetic evolution of late Cenozoic, post-collision volcanism in western Anatolia, Turkey. *J. Volcanol. Geotherm. Res.* **2000**, *102*, 67–95. [CrossRef]
54. Alvaro, J.J.; Pouclet, A.; Ezzouhairi, H.; Abderrahmane, S. Early Neoproterozoic rift-related magmatism in the Anti-Atlas margin of the West African craton, Morocco. *Precambrian Res.* **2014**, *255*, 433–442. [CrossRef]
55. Zheng, H.; Huang, Q.T.; Kapsiotis, A.; Xia, B. Early cretaceous ophiolites of the Yarlung Zangbo Suture Zone: Insights from dolerites and peridotites from the Baer upper mantle suite, SW Tibet (China). *Int. Geol. Rev.* **2017**, *59*, 1–19. [CrossRef]
56. Yang, G.X.; Li, Y.J.; Xiao, W.J.; Sun, Y. Petrogenesis and tectonic implications of the middle Silurian volcanic rocks in northern West Junggar, NW China. *Int. Geol. Rev.* **2014**, *56*, 869–884. [CrossRef]
57. Kouankap, D.; Pierre, W.; Mufur, A.M.; Ganno, S. Contrasting Ba-Sr Granitoids from Bamenda Area, NW Cameroon: Sources Characteristics and Implications for the Evolution of the Pan African Fold Belt. *J. Geosci. Geomat.* **2018**, *6*, 65–76. [CrossRef]
58. Ye, X.Q.; Xu, Z.T.; Sun, L.Y.; Li, Z.W.; Li, M.M.; Jia, L. Genesis and Tectonic Significance of Miocene Tephrite in Laohushan Volcanic Area, Jilin Province. *Earth Sci.* **2024**, *49*, 1352–1366. (In Chinese with English abstract)
59. Bu, T.; Wang, G.Q.; Huang, B.T.; Guo, L.; Zou, X. Petrogenesis and tectonic significances of Early Devonian granites in Huangqiuquan area from the northern Beishan Orogenic Belt, NW China. *Geol. Rev.* **2024**, *70*, 2193–2211. (In Chinese with English abstract) [CrossRef]
60. Chappell, B.W. Aluminium saturation in I- and S-type granites and the characterization of fractionated haplogranites. *Lithos* **1999**, *46*, 535–551. [CrossRef]
61. Bonin, B. A-Type Granites and Related Rocks: Evolution of a Concept, Problems and Prospects. *Lithos* **2007**, *97*, 129. [CrossRef]
62. Pitcher W, S. Granite type and tectonic environment. *Mt. Build. Process.* **1982**, *4*, 19–40.
63. Chappell, B.W.; White, A.J.R. I-and S-type granites in the Lachlan fold belt. *Earth Environ. Sci. Trans. R. Soc. Edinb.* **1992**, *83*, 1–26. [CrossRef]
64. Wu, F.Y.; Li, X.H.; Yang, J.H.; Zheng, Y.F. Discussions on the petrogenesis of granites. *Acta Petrol. Sin.* **2007**, *23*, 1217–1238. (In Chinese with English abstract)
65. Wu, F.Y.; Liu, X.C.; Ji, W.Q.; Wang, J.M.; Yang, L. Highly fractionated granites: Recognition and research. *Sci. China Earth Sci.* **2017**, *60*, 1201–1219. (In Chinese with English abstract) [CrossRef]
66. Breiter, K.; Lamarão, C.N.; Borges, R.M.K.; Dall'Agnol, R. Chemical characteristics of zircon from A-type granites and comparison to zircon of S-type granites. *Lithos* **2014**, *192*, 208–225. [CrossRef]
67. Wu, F.Y.; Jahn, B.M.; Wilde, S.A.; Lo, C.H.; Yui, T.F.; Lin, Q.; Ge, W.C.; Sun, D.Y. Highly fractionated I-type granites in NE China (I): Geochronology and petrogenesis. *Lithos* **2003**, *66*, 241–273. [CrossRef]
68. Xia, R.; Wang, C.M.; Qing, M.; Li, W.; Carranza, E.J.M.; Guo, X.; Zeng, G.Z. Zircon U-Pb dating, geochemistry and Sr-Nd-Pb-Hf-O isotopes for the Nangetan granodiorites and mafic microgranular enclaves in the East Kunlun Orogen: Record of closure of the Paleo-Tethys. *Lithos* **2015**, *234*, 47–60. [CrossRef]
69. Shao, F.L.; Niu, Y.L.; Liu, Y.; Chen, S.; Kong, J.J.; Duan, M. Petrogenesis of Triassic granitoids in the East Kunlun Orogenic Belt, northern Tibetan Plateau and their tectonic implications. *Lithos* **2017**, *282*, 33–44. [CrossRef]
70. Defant, M.J.; Drummond, M.S. Derivation of some modern arc magmas by melting of young subducted lithosphere. *Nature* **1990**, *347*, 662–665. [CrossRef]
71. Taylor, S.R.; Mclennan, S.M. *The Continental Crust: Its Composition and Evolution: An Examination of the Geochemical Record Preserved in Sedimentary Rocks*; Backwell Scientific Publications: Boston, MA, USA, 1985; pp. 209–230.
72. Rapp, R.P.; Watson, E.B. Dehydration melting of metabasalt at 8–32 kbar: Implications for continental growth and crust-mantle recycling. *J. Petrol.* **1995**, *36*, 891–931. [CrossRef]
73. Jung, S.; Pfänder, J.A. Source composition and melting temperatures of orogenic granitoids: Constraints from CaO/Na_2O, $A1_2O_3/TiO_2$ and accessory mineral saturation thermometry. *Eur. J. Mineral.* **2007**, *19*, 859–870. [CrossRef]
74. Lassiter, J.C.; DePaolo, D.J. Plume/Lithosphere Interaction in the Generation of Continental and Oceanic Flood Basalts: Chemical and Isotopic Constraints. In *Large Igneous Provinces: Continental, Oceanic, and Planetary Flood Volcanism*; Mahoney, J.J., Coffin, M.F., Eds.; American Geophysical Union: Washington, DC, USA, 1997; pp. 335–356. [CrossRef]
75. Cawood, P.A.; Hawkesworth, C.J.; Dhuime, B. The continental record and the generation of continental crust. *Geol. Soc. Am. Bull.* **2013**, *125*, 14–32. [CrossRef]
76. Niu, Y.Z.; Li, C.Y.; Shi, G.R.; Lu, J.C.; Xu, W.; Shi, J.Z. Unconformity-bounded Upper Paleozoic megasequences in the Beishan Region (NW China) and implications for the timing of the Paleo-Asian Ocean closure. *J. Asian Earth Sci.* **2018**, *167*, 11–32. [CrossRef]
77. Cawood, P.A.; Kröner, A.; Collins, W.J.; Kusky, T.M.; Mooney, W.D.; Windley, B.F. Accretionary orogens through Earth history. *Geol. Soc. Lond. Spec. Publ.* **2009**, *318*, 1–36. [CrossRef]
78. Wang, Y.L.; Zhang, C.J.; Xiu, S.Z. Th/Hf-Ta/Hf identification of tectonic setting of basalts. *Acta Petrol. Sin.* **2001**, *17*, 413–421. (In Chinese with English abstract)

79. Collins, W.J.; Belousova, E.A.; Kemp, A.I.; Murphy, J.B. Two contrasting Phanerozoic orogenic systems revealed by hafnium isotope data. *Nat. Geosci.* **2011**, *4*, 333–337. [CrossRef]
80. Ding, J.; Han, C.; Xiao, W.; Wang, Z.; Song, D. Geochronology, geochemistry and Sr-Nd isotopes of the granitic rocks associated with tungsten deposits in Beishan district, NW China, Central Asian Orogenic Belt: Petrogenesis, metallogenic and tectonic implications. *Ore Geol. Rev.* **2017**, *89*, 441–462. [CrossRef]
81. Cawood, P.A.; Leitch, E.C.; Merle, R.E.; Nemchin, A.A. Orogenesis without collision: Stabilizing the Terra Australis accretionary orogen, eastern Australia. *Geol. Soc. Am. Bull.* **2011**, *123*, 2240–2255. [CrossRef]
82. Pearce, J.A.; Norry, M.J. Petrogenetic implications of Ti, Zr, Y, and Nb variations in volcanic rocks. *Contrib. Mineral. Petrol.* **1979**, *69*, 33–47. [CrossRef]
83. Pearce, J.A.; Harris, N.B.W.; Tindle, A.G. Trace element discrimination diagrams for the tectonic interpretation of granitic rocks. *J. Petrol.* **1984**, *25*, 956–983. [CrossRef]
84. Harris, N.B.W.; Pearce, J.A.; Tindle, A.G. Geochemical characteristics of collision-zone magmatim, collision tectonics. *Geol. Soc. Lond. Spec. Publ.* **1986**, *19*, 67–81. [CrossRef]
85. Song, D.; Xiao, W.; Windley, B.F.; Han, C.; Tian, Z. A Paleozoic Japan-type subduction-accretion system in the Beishan orogenic collage, southern Central Asian Orogenic Belt. *Lithos* **2015**, *224*, 195–213. [CrossRef]
86. Liang, J.W.; Chen, Y.L.; Zhang, W.Q.; Wang, G.Q.; Yu, J.Y.; Li, X.M. Detrital Zircon Dating of Devonian and Geological Significance of the Devonian Sangejing Formation in Beishan Area, Gansu Province. *Geol. Sci. Technol. Inf.* **2014**, *33*, 1–9. (In Chinese with English abstract)
87. Song, D.; Xiao, W.; Han, C.; Tian, Z.H. Polyphase deformation of a Paleozoic forearc–arc complex in the Beishan orogen, NW China. *Tectonophysics* **2014**, *632*, 224–243. [CrossRef]
88. Cleven, N.; Lin, S.F.; Guilmette, C.; Xiao, W.J.; Davis, B. Petrogenesis and implications for tectonic setting of Cambrian supra subduction-zone ophiolitic rocks in the central Beishan orogenic collage, Northwest China. *J. Asian Earth Sci.* **2015**, *113 Pt 1*, 369–390. [CrossRef]
89. Mao, Q.G.; Xiao, W.J.; Ao, S.J.; Yang, H. Subduction Initiation of the Southern Branch of the Paleo-Asian Ocean in the Middle Ordovician in the Southern Beishan Orogen. *Earth Space Sci.* **2023**, *10*, e2022EA002350. [CrossRef]
90. Yu, J.Y.; Li, X.G.; Wang, G.Q.; Wu, P.; Yan, Q.J. Zircon U-Pb ages of Huitongshan and Zhangfangshan ophiolite in Beishan of Gansu-Inner Mongolia border area and their significance. *Geol. Bull. China* **2012**, *31*, 2038–2045. (In Chinese with English abstract)
91. Meng, Y.; Zhang, X.; Bai, J.; Wang, K.; Qi, Y.; Zhao, H.; Han, Y. Petrogenesis and Geochronology of the Shazuoquan Ophiolite, Beishan Orogenic Belt: Constraints on the Evolution of the Beishan Ocean. *Minerals* **2023**, *13*, 1067. [CrossRef]
92. Wiedenbeck, M.; Hanchar, J.M.; Peck, W.H.; Sylvester, P.; Vley, J.; Whitehouse, M.; Kronz, A.; Morishita, Y.; Nasdala, L.; Fie-big, J.; et al. Further characterization of the 91500-zircon crystal. *Geostand. Geoanal. Res.* **2004**, *28*, 9–39. [CrossRef]
93. Pearce, N.J.G.; Perkins, W.T.; Westgate, J.A.; Gorton, M.P.; Chenery, S.P. A Compilation of New and Published Major and Trace Element Data for NIST SRM 610 and NIST SRM 612 Glass Reference Materials. *Geostand. Newsl.* **1997**, *21*, 115–144. [CrossRef]
94. Jackson, S.E.; Pearson, N.J.; Griffin, W.L.; Belousova, E.A. The application of laser ablation-inductively coupled plasma-mass spectrometry to in situ U–Pb zircon geochronology. *Chem. Geol.* **2004**, *211*, 47–69. [CrossRef]
95. Vermeesch, P. IsoplotR: A free and open toolbox for geochronology. *Geosci. Front.* **2018**, *9*, 1479–1493. [CrossRef]
96. Yuan, H.L.; Gao, S.; Liu, X.M.; Li, H.M.; Gunther, D.; Wu, F.Y. Accurate U–Pb age and trace element determinations of zircon by laser ablation-inductively coupled plasma-mass spectrometry. *Geostand. Geoanal. Res.* **2004**, *28*, 353–370. [CrossRef]
97. Söderlund, U.; Patchett, P.J.; Vervoort, J.D.; Isachsen, C.E. The 176Lu decay constant determined by Lu–Hf and U–Pb isotope systematics of Precambrian mafic intrusions. *Earth Planet. Sci. Lett.* **2004**, *219*, 311–324. [CrossRef]
98. Bouvier, A.; Vervoort, J.D.; Patchett, P.J. The Lu–Hf and Sm–Nd isotopic composition of CHUR: Constraints from unequili-brated chondrites and implications for the bulk composition of terrestrial planets. *Earth Planet. Sci. Lett.* **2008**, *273*, 48–57. [CrossRef]
99. Nowell, G.M.; Kempton, P.D.; Noble, S.R.; Fitton, J.G.; Saunders, A.D.; Mahoney, J.J.; Taylor, R.N. High precision Hf isotope measurements of MORB and OIB by thermal isnisation mass spectrometry: Insights into the depleted mantle. *Chem. Geol.* **1998**, *149*, 211–233. [CrossRef]
100. Griffin, W.L.; Pearson, N.J.; Belousova, E.; Jackson, S.E.; van Achterbergh, E.; O'Reilly, S.Y.; Shee, S.R. The Hf isotope composition of cratonicmantle: LA-MC-ICPMS analysis of zircon megacrysts in kimberlites. *Geochim. Cosmochim. Acta* **2000**, *64*, 133–147. [CrossRef]
101. Blichert-Toft, J.; Albarede, F. The Lu-Hf geochemistry of chondrites and the evolution of the mantle-crust system. *Earth Planet. Sci. Lett.* **1997**, *148*, 243–258. [CrossRef]
102. Bao, Z.A.; Chen, L.; Zong, C.L.; Yuan, H.L.; Chen, K.Y.; Dai, M.N. Development of pressed sulfide powder tablets for in situ sulfur and lead isotope measurement using LA-MC-ICP-MS. *Int. J. Mass Spectrom.* **2017**, *421*, 255–262. [CrossRef]

103. Li, X.H.; Liu, Y.; Tu, X.L.; Hu, G.Q.; Zeng, W. Precise determination of chemical compositions in silicate rocks using ICP-AES and ICP-MS: A comparative study of sample digestion techniques of alkali fusion and acid dissolution. *Geochemical* **2002**, *31*, 289–294.
104. Gao, J.J.; Liu, J.H.; Li, X.G.; Yan, Q.S.; Wang, X.J.; Wang, H.M. The determination of 52 elements in marine geological samples by an inductively coupled plasma optical emission spectrometry and an inductively coupled plasma mass spectrometry with a high-pressure closed digestion method. *Acta Oceanol. Sin.* **2017**, *36*, 113–121. [CrossRef]

Disclaimer/Publisher's Note: The statements, opinions and data contained in all publications are solely those of the individual author(s) and contributor(s) and not of MDPI and/or the editor(s). MDPI and/or the editor(s) disclaim responsibility for any injury to people or property resulting from any ideas, methods, instructions or products referred to in the content.